



HAL
open science

Brain Structure Ages - A new biomarker for multi-disease classification

Huy-Dung Nguyen, Michaël Clément, Boris Mansencal, Pierrick Coupé

► **To cite this version:**

Huy-Dung Nguyen, Michaël Clément, Boris Mansencal, Pierrick Coupé. Brain Structure Ages - A new biomarker for multi-disease classification. *Human Brain Mapping*, 2024, 45 (1), 10.1002/hbm.26558 . hal-04080401v2

HAL Id: hal-04080401

<https://hal.science/hal-04080401v2>

Submitted on 10 Dec 2023

HAL is a multi-disciplinary open access archive for the deposit and dissemination of scientific research documents, whether they are published or not. The documents may come from teaching and research institutions in France or abroad, or from public or private research centers.

L'archive ouverte pluridisciplinaire **HAL**, est destinée au dépôt et à la diffusion de documents scientifiques de niveau recherche, publiés ou non, émanant des établissements d'enseignement et de recherche français ou étrangers, des laboratoires publics ou privés.



Distributed under a Creative Commons Attribution - NonCommercial - NoDerivatives 4.0 International License

RESEARCH ARTICLE

Brain Structure Ages - A new biomarker for multi-disease classification

Huy-Dung Nguyen | Michaël Clément | Boris Mansencal | Pierrick Coupé

¹Univ. Bordeaux, CNRS, Bordeaux INP, LaBRI,
UMR 5800, 33400 Talence, France

Correspondence

Corresponding author Huy-Dung Nguyen.
Email: huy-dung.nguyen@u-bordeaux.fr

Abstract

Age is an important variable to describe the expected brain's anatomy status across the normal aging trajectory. The deviation from that normative aging trajectory may provide some insights into neurological diseases. In neuroimaging, predicted brain age is widely used to analyze different diseases. However, using only the brain age gap information (*i.e.*, the difference between the chronological age and the estimated age) can be not enough informative for disease classification problems. In this paper, we propose to extend the notion of global brain age by estimating brain structure ages using structural magnetic resonance imaging. To this end, an ensemble of deep learning models is first used to estimate a 3D aging map (*i.e.*, voxel-wise age estimation). Then, a 3D segmentation mask is used to obtain the final brain structure ages. This biomarker can be used in several situations. First, it enables to accurately estimate the brain age for the purpose of anomaly detection at the population level. In this situation, our approach outperforms several state-of-the-art methods. Second, brain structure ages can be used to compute the deviation from the normal aging process of each brain structure. This feature can be used in a multi-disease classification task for an accurate differential diagnosis at the subject level. Finally, the brain structure age deviations of individuals can be visualized, providing some insights about brain abnormality and helping clinicians in real medical contexts.

KEYWORDS

Brain Structure Ages, Age prediction, Deep learning, Multi-disease Classification, Alzheimer's disease, Frontotemporal dementia, Multiple sclerosis, Parkinson's disease, Schizophrenia

1 | INTRODUCTION

In the medical field, chronological age is widely used as an indicator to describe people. It depicts a reference curve that healthy organs should follow. The deviation from that reference may be associated with different factors such as the interaction of genes, environment, lifestyle, and diseases¹. To measure this deviation, the concept of biological age (BA) has been created. It is an estimation of individual's age based on various advanced strategies^{2,3,4} and is expected to be able to take into account all the factors mentioned above. Consequently, an accelerated (or delayed) aging process results in a higher (or lower) value of BA with respect to chronological age.

The analysis of BA can be associated with a whole-body system or a specific organ. The whole-body evaluation approaches typically use non-imaging data (*e.g.*, DNA methylation patterns⁵, protein⁶) but often struggle to account for variations in aging among individual organs⁷. To this end, Tian *et al.* recently proposed a novel approach employing multimodal brain imaging, physiological measurements, and blood phenotypes to construct a multiorgan aging network⁸. Their research unveiled the heterogeneous nature of organ aging, and the multiorgan aging network could potentially facilitate early identification of individuals at risk of age-related morbidity. Besides, investigations focused on BA for specific organs are also of great interest. Le Gallec *et al.* proposed to use the prediction of liver and pancreas ages based on imaging data to improve the estimation of abdominal age⁹. In another study, Mauer *et al.* employed 3D knee imaging to estimate age and used it to achieve accurate majority classification (individuals older than 18 years of age)¹⁰.

Among the various organs studied, the brain emerges as a prominent subject of research. Brain structure changes are demonstrated to be mutually caused by the natural aging process and neurodegenerative diseases^{11,12,13,14,15,16}. Cole *et al.* demonstrated that biological brain age can enable the development of treatment plans and a better understanding of disease processes¹⁷. The authors emphasized that the difference between the predicted brain age and the chronological age is a valuable bio-marker since it shows a correlation with aging as well as with diseases. This difference is denoted as BrainAGE for Brain Age Gap Estimation. Since its introduction, this new bio-marker has been widely used in many studies to analyze various diseases¹. Generally, a model is trained with brain images from a healthy population and then used to estimate the age of patients with diseases.

In BrainAGE, structural magnetic resonance imaging (sMRI) is the most used modality (about 88% of studies¹⁸). It has been shown that reasonable prediction error can be achieved using this modality. Moreover, sMRI is commonly available in medical environments¹⁸. Initially, sMRI was used with some traditional machine learning algorithms such as relevance vector regression¹⁹, support vector regression²⁰, and Gaussian process regression²¹ to perform BrainAGE. The prediction error of these methods ranges from 4.29 to 5.02 years for the mean absolute error (MAE) metric. Since the success of deep learning in many natural image processing applications, it has also become a useful technique in various medical imaging studies. Recent studies show the capacity of deep learning algorithms in the brain age estimation task based on sMRI with an MAE ranging from 1.96 to 4.16 years^{7,22,23,24,25}. These promising results suggest using deep learning to estimate brain age for further analysis.

These deep learning-based methods adapt famous convolutional neural network (CNN) architectures to estimate brain age. When employing a VGG-like architecture, Ueda *et al.* demonstrated that using 3D CNN can lead to better accuracy than 2D CNN for age prediction²⁶. In another work, Cole *et al.* also used a VGG-like architecture and found that the grey matter extracted from 3D sMRI is better than white matter and raw image for age prediction¹⁷. Using a similar architecture, Bermudez *et al.* suggested additionally taking advantage of brain structure volume to improve the model performance²⁵. Binti *et al.* employed ResNet architecture to predict age on several sub-volumes of brain image²⁷. The final prediction was aggregated using a linear regression model. Armanious *et al.* proposed to use the inception module with squeeze-and-excitation module to accurately predict healthy brain age⁷. Bashyam *et al.* customized the inception-resnetv2 to build their model and trained it on 11729 healthy subjects.

After training a brain age prediction model, the next step is to apply it to a population of interest to compare healthy and diseased groups (*i.e.*, analysis at the population level). For example, Franke *et al.* analyzed brain maturation during childhood and adolescence²⁸. By applying a trained model on subjects being born before the 28th and after the 29th week of gestation, they found that the BrainAGE of the first group was significantly lower than the second group, showing a delayed structural brain maturation of the first group. Applying the same technique, Koutsouleris *et al.* demonstrated an accelerated aging of 5.5 years in schizophrenia and 4.0 years in major depression patients compared to normal aging²⁹. In another study dedicated to Alzheimer's Disease (AD), the BrainAGE was estimated at about +10 years in AD patients, implying accelerated aging of this population¹⁹.

Although BrainAGE can provide a description of a specific population, its application in individual diagnosis is still limited. Only a few works suggested performing disease detection or differential diagnosis using BrainAGE at the subject level. For instance, the BrainAGE was used as a biomarker to perform differential diagnosis between mild cognitive impairment and AD in³⁰ and to diagnose AD (*i.e.*, AD patients *vs.* healthy controls) in^{31,32}. More recently, Cheng *et al.* used deep learning to accurately predict brain age and they use BrainAGE as the only feature for various binary diagnosis tasks (*i.e.*, diseased subjects *vs.* healthy subjects)³³. Although encouraging results were obtained, these works performed only binary classification tasks but not multi-class classification. The reason for this may be due to the coarse description of the brain's state provided by the global BrainAGE. Indeed, BrainAGE can only describe the aging process of the whole brain but does not provide any details about brain structures' state. Therefore, it is difficult to use BrainAGE for involved tasks such as the differential diagnosis of multiple pathologies.

Since global age estimation, several approaches have proposed voxel-wise estimations. Beheshti *et al.* introduced a methodology that estimates brain age at the voxel level based on patch similarity³⁴. The global brain age was subsequently deduced using a weighted average of the predicted voxels, achieving an MAE of 1.66 years. This method highlights the potential of voxel-wise age prediction. In another study, Popescu *et al.* employed a U-Net model to estimate brain age at the voxel level, using data from gray and white matter in sMRI scans³⁵. Although their technique did not surpass other models in age estimation accuracy, this approach did reveal significant differences in local brain ages between healthy individuals and dementia patients, presenting a promising avenue for future research in brain disease diagnosis.

In this paper, we propose to extend the notion of the global brain age to local brain structure ages. Our main hypothesis is that the aging process is heterogeneous over the brain and specifically, different brain structures may present different ages. While voxel-wise age estimation methods might be valuable markers, our paper introduces a novel structure age estimation as a complementary method dedicated to interpretable computer-aided diagnosis. Structure age summarizes the brain's state into a

vector of apparent ages for multiple anatomical structures, which is easier to interpret than voxel-wise ages. This summary not only provides a quick comparative assessment of the structural impacts of diseases but also reduces the complexity of data analysis. By doing so, it helps prevent model overfitting, facilitates the integration with other structure-based biomarkers (*e.g.*, volume) in disease classification, and provides more robust estimates by averaging noisy voxel-level estimations. Consequently, we first estimate the brain age at the voxel level. This results in a 3D aging map of voxelwise brain ages. By averaging predicted brain ages by brain structure, we obtain the Brain Structure Ages, denoted as BSA. This local BSA is expected to provide more information about the subject's condition than a global age prediction of a whole subject's brain. As shown later, this novel biomarker can be used as input of a support vector regressor (SVR) to accurately estimate the subject's age. During validation, our framework showed competitive results compared to state-of-the-art methods. Furthermore, the difference between BSA and the subject's chronological age, denoted as BSAGE for Brain Structure Age Gap Estimation, can be also used with a support vector machine classifier (SVM) for multi-class classification (*i.e.*, Cognitively Normal (CN) *vs.* AD *vs.* Frontotemporal Disease (FTD) *vs.* Multiple Sclerosis (MS) *vs.* Parkinson's disease (PD) *vs.* Schizophrenia (SZ)). In our experiments, we demonstrated the important gain of using BSAGE compared to BrainAGE for the multi-disease classification task. Finally, by projecting the BSAGE on a brain atlas, we can visually observe the brain regions affected by different diseases.

2 | MATERIALS

2.1 | Datasets

The data used in this study comprise 39255 images from various datasets: the Autism Brain Imaging Data Exchange (ABIDE)^{36,37}, the Alzheimer's Disease Neuroimaging Initiative (ADNI)³⁸, the Australian Imaging Biomarkers and Lifestyle Study of aging (AIBL)³⁹, the International Consortium for Brain Mapping (ICBM)⁴⁰, the Information eXtraction from Images (IXI)[‡], the National Database for Autism Research (NDAR)⁴¹, the Open Access Series of Imaging Studies (OASIS)⁴², Cincinnati MR Imaging of Neurodevelopment (C-MIND)[§], UKBioBank⁴³, the Strategic Research Program for Brain Sciences (SRPBS)⁴⁴, the Center for Biomedical Research Excellence (COBRE)[¶], the Cambridge Centre for aging and Neuroscience (CamCAN)⁴⁵, the Parkinson's Progression Markers Initiative (PPMI)⁴⁶, the Frontotemporal Lobar Degeneration Neuroimaging Initiative (NIFD)[#], the Observatoire Français de la Sclérose en Plaques (OFSEP)⁴⁷, the National Alzheimer's Coordinating Center (NACC)⁴⁸, the Dallas Lifespan Brain Study (DLBS)^{||}, the Minimal Interval Resonance Imaging in Alzheimer's Disease⁴⁹, the Minimal Interval Resonance Imaging in Alzheimer's Disease (MIRIAD)⁴⁹, and a study on schizophrenia (BrainGluSchi)⁵⁰. All the T1 weighted images at the baseline were used.

2.1.1 | Chronological age prediction

Among available data, 32718 images were used to study the accuracy of our chronological age predictor. First, eight datasets including 2887 images (*i.e.*, ABIDE I, ADNI, AIBL, ICBM, C-MIND, IXI, NDAR, OASIS1) were used in training/validation. Second, two external datasets (*i.e.*, out-of-domain) were used for testing. Concretely, CN subjects of ABIDE II (*i.e.*, 580 images) were used to estimate the model accuracy on a young population and CN from UKBioBank (*i.e.*, 29251 images) were used to estimate the model accuracy on an older population (see Table 1). For ABIDE, we ensured that no subject in phase I was presented in phase II.

2.1.2 | Multiple pathologies classification

Besides, we assessed the classification performance using BSAGE on 6537 images composed of 6 classes (*i.e.*, CN, AD, FTD, MS, PD and SZ). Eight datasets including 1992 images (ADNI, AIBL, SRPBS, COBRE, CamCAN, PPMI phase 1, NIFD and OFSEP centers 1-2) were used to perform a 10-fold cross validation (in-domain validation) (see Table 2). Then, we constructed

‡ <https://brain-development.org/ixi-dataset/>

§ https://nda.nih.gov/edit_collection.html?id=2329

¶ http://fcon_1000.projects.nitrc.org/indi/retro/cobre.html

<https://ida.loni.usc.edu/collaboration/access/appLicense.jsp>

|| https://fcon_1000.projects.nitrc.org/indi/retro/dlbs.html

an out-of-domain dataset including 4545 images using seven cohorts (*i.e.*, NACC, DLBS, MIRIAD, OASIS3, BrainGluShi, PPMI phase 2 and OFSEP-other-centers) to assess the generalization capacity of such models. For the OFSEP, we used the acquisition sites to split this global dataset into two non-overlapping domains. For PPMI, we ensured that no subject in phase I was presented in phase II.

TABLE 1 On top, summary of participants used for training age predictor. On bottom, description of the external datasets used for testing.

| Usage | Dataset | Male/Female | Age (Mean \pm Std) |
|--------------------------|--------------|-------------|----------------------|
| Age prediction training | ABIDE I | 408/84 | 17.5 \pm 7.8 |
| | ADNI | 201/203 | 74.8 \pm 5.8 |
| | AIBL | 112/120 | 72.3 \pm 6.7 |
| | ICBM | 112/182 | 33.7 \pm 14.3 |
| | C-MIND | 107/129 | 8.4 \pm 4.3 |
| | IXI | 242/307 | 48.8 \pm 16.5 |
| | NDAR | 208/174 | 12.4 \pm 6.0 |
| | OASIS1 | 111/187 | 45.3 \pm 23.8 |
| Young population testing | ABIDE II | 403/177 | 14.8 \pm 9.3 |
| Older population testing | UKBioBank | 14917/14334 | 64.2 \pm 7.9 |
| | Total | 16821/15897 | 14.8 \pm 9.3 |

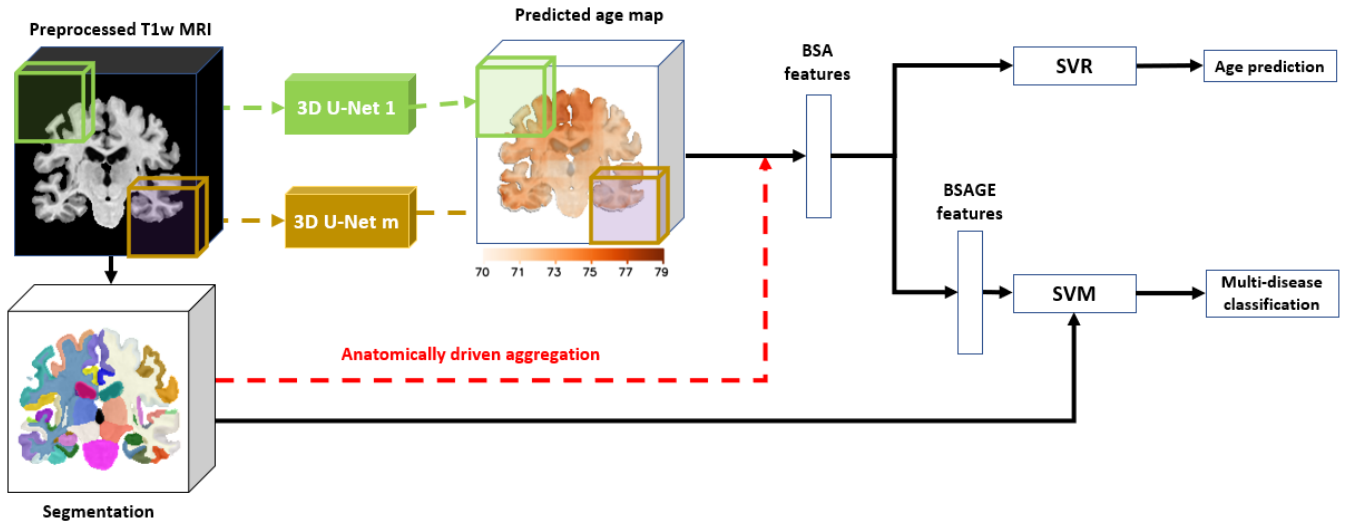


FIGURE 1 An overview of the proposed method. The T1w image, its segmentation and the age map are taken from a 71 years old healthy person.

2.2 | Preprocessing

The preprocessing procedure is composed of five steps: (1) denoising image⁵¹, (2) inhomogeneity correction⁵², (3) affine registration into the MNI152 space ($181 \times 217 \times 181$ voxels at $1mm \times 1mm \times 1mm$)⁵³, (4) intensity standardization⁵⁴ and (5)

TABLE 2 Number of participants (Male/Female) used for multi-class classification.

| Usage | Dataset | CN | AD | FTD | MS | PD | SZ |
|---|---------------------------|---------|---------|--------|----------|----------|--------|
| In-domain: 10-fold cross-validation training set | ADNI | | 181/150 | | | | |
| | AIBL | | 18/28 | | | | |
| | SRPBS | 88/60 | | | | | 84/58 |
| | COBRE | 11/7 | | | | | 54/14 |
| | CamCAN | 75/85 | | | | | |
| | PPMI phase 1 | 35/13 | | | | 228/131 | |
| | NIFD | 15/15 | | | 87/56 | | |
| | OFSEP centers 1-2 | | | | | 161/338 | |
| | NACC | 47/104 | 318/419 | 22/23 | | | |
| | DLBS | 117/196 | | | | | |
| Out-of-domain: independent testset | MIRIAD | 12/11 | 19/27 | | | | |
| | OASIS3 | 270/385 | 46/46 | | | | |
| | Brain- GluSchi | 61/25 | | | | | 71/11 |
| | PPMI phase 2 | | | | | 74/58 | |
| | OFSEP other centers | | | | | 585/1598 | |
| | Total | 731/901 | 582/670 | 109/79 | 746/1936 | 302/189 | 209/83 |

intracranial cavity (ICC) extraction⁵⁵. After preprocessing, we used AssemblyNet^{** 56} to get the parcellation of the brain into 133 structures (see Figure 1). This brain structure segmentation is then used to compute the BSA for further analysis.

3 | METHOD

3.1 | Method overview

Figure 1 provides an overview of our method. First, we estimate the brain ages map at voxel level from a preprocessed T1 image using a large number of U-Nets. Then, this 3D map is used with a segmentation mask to compute the BSA features (Section 3.1.1). Finally, the BSA features can be employed to estimate the chronological age using an SVR model or combined with brain structure volumes to perform multi-disease classification using an SVM classifier (Section 3.1.2).

3.1.1 | Brain structure age estimation

In order to produce the 3D aging map, we extracted $m = k^3$ overlapping 3D sub-volumes of the same size for each T1w MRI. Next, we trained m U-Nets to predict age at voxel level with these m 3D sub-volumes. The goal of this training strategy is dual. First, as the size of a sub-volume is relatively small compared to the original image, it can be trained with a lighter weight model and thus, require only a low computation capacity. Second, we limit the receptive field of each model to a local brain region in order to force it to locally describe the brain age. The outputs were then used to reconstruct a 3D brain age map. Finally, the

** Available at <https://github.com/volBrain/AssemblyNet>

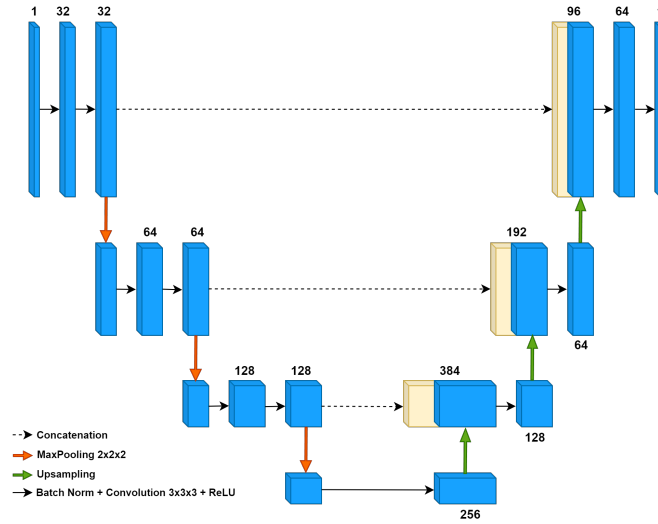


FIGURE 2 Architecture of a unit U-Net used for voxel-level age prediction. The number above each block is the number of channel.

BSA was computed with the help of an AssemblyNet-based brain segmentation⁵⁶. In practice, we estimated the mean value of voxel-wise age estimation for each structure segmentation.

3.1.2 | Application to chronological age prediction and multi-disease classification

To demonstrate different use cases of the BSA, we performed two experiments using this biomarker: chronological age prediction which can help to briefly describe a population and multi-disease classification which can guide clinicians to focus on certain pathologies.

To predict the chronological age of healthy people, we employed a classical SVR and used the predicted BSA as its input. For the multi-disease classification, we first computed the BSAGE (*i.e.*, the difference between BSA and the subject's chronological age) and then used it as input of an SVM classifier to address the 6-class problem CN vs. AD vs. FTD vs. MS vs. PD vs. SZ. Moreover, structure volume is used as additional feature of BSAGE for SVM-based classification.

3.2 | Implementation details

First, a preprocessed T1w MRI in the MNI space of size $181 \times 217 \times 181$ voxels at $1mm^3$ was downsampled with a factor of 2 to the size of $91 \times 109 \times 91$ voxels. After that, we extract k^3 (*i.e.*, $k = 5$) overlapping sub-volumes of the same size $32 \times 48 \times 32$ voxels and evenly distributed along the 3 image's dimensions from the downscale image. We trained $m = k^3$ (*i.e.*, $m = 125$) U-Nets to predict age at voxel level with these m sub-volumes. Figure 2 shows the architecture of our unit U-Net used for voxel-level age prediction. The m outputs were then used to reconstruct a 3D age map of size $91 \times 109 \times 91$ voxels. Of note, the predicted brain age located at overlapping voxel positions of more than 1 sub-volume was averaged. The reconstructed image was upsampled using trilinear interpolation to the same spatial size as the original input. This 3D map was used to compute BSA and then BSAGE features.

For training the U-Nets, each voxel inside the ICC is assigned the subject's chronological age as its ground truth value, while all other voxels are set to zero. During training, we use the mean absolute error (MAE) as loss function and SGD optimizer. The batch size is set to 8 and the training was terminated after 20 epochs without any improvement on validation loss. The first U-Net was trained from scratch and other U-Nets were trained with transfer learning from their adjacent U-Net (see⁵⁶ for more details). The training data is split into training/validation sets with a ratio of 80%/20% (see Table 1). In addition, when a new U-Net was trained, the training and validation data were gathered and re-split to exploit the maximum information from available data. Finally, we employed different data augmentation techniques to alleviate the overfitting problem. Concretely, we

randomly shifted a patch by $t \in \{-1, 0, 1\}$ voxel in each dimension (denoted as random shift technique) and then applied mixup data augmentation⁵⁷.

Before using BSA features, we applied an age correction technique for each of their elements. We followed a simple method of Smith *et al.*⁵⁸ to eliminate bias in each structure brain age. Concretely, we denoted the actual age as Y (an $N_{subjects} \times 1$ vector), the brain age as Y_B , a brain structure age as X_s (an $N_{subjects} \times 1$ vector) and the bias term δ . So, we predicted Y_B from X_s : $Y_B = Y + \delta = X_s\beta$. This is equivalent to $Y = X_s\beta - \delta$. This regression can be solved with $\beta = (X_s^T X)^{-1} X_s^T Y$. Finally, $Y_B = X_s(X_s^T X)^{-1} X_s^T Y$.

When training the SVR to estimate chronological age, three kernels were used to select the best model through our cross-validation: linear, polynomial and radial basis function. Five values of C and epsilon in [0.1, 1, 10, 100, 1000] were used in the hyper-parameter search. We performed a grid-search for the kernel and the hyper-parameters C, epsilon.

When training the SVM for multi-disease classification, "one vs rest" was used as the decision function shape, three kernels were used to select the best model through our cross-validation: linear, polynomial and radial basis function. One hundred values of C in the log-space [-1.5; 0.5] were used in the hyper-parameter search. We performed a grid-search for the kernel and the hyper-parameter C.

3.3 | Validation Framework

For chronological age prediction, we compute the BSA features of U-Nets' training subjects. This data is used to train the SVR-based regression (10-fold cross-validation). This results in 10 SVR models. We used two separate out-of-domain datasets to assess our method accuracy (see Table 1). When evaluating the framework for this data (young and old populations), we used these 10 models to predict the individual chronological age and then averaged the 10 obtained results to make only one prediction per subject.

For multi-disease classification, we employed a 10-fold cross-validation for training our SVM classifier, as outlined in Table 2. Each of the 10 models was evaluated using its corresponding test fold. Consequently, each test sample was assessed once, yielding a single global final prediction. We concatenated the results across 10 test folds to determine the in-domain performance of our model. Furthermore, we examined the model's generalizability by testing it on an out-of-domain dataset, also detailed in Table 2. For this external data set, each test sample was evaluated using all 10 cross-validated models, and their outputs were averaged to enhance model generalization. This resulted in one final prediction for each test sample in the out-of-domain dataset.

4 | EXPERIMENTAL RESULTS

4.1 | Chronological age estimation

4.1.1 | Ablation study

In this part, we aim at studying different factors influencing the model performance: Data amount, different augmentation strategies (*e.g.*, random shift, mixup⁵⁷), age correction technique (see Section 3.2) and regressor (*e.g.*, Multi-Layer Perceptron (MLP), SVR). Table 3 shows the comparison results. The regression lines are provided in the Annexes.

First, we can observe that increasing the data amount (exp. 1, 2, 3) consistently improve the model accuracy on both young and old population in all metrics (*i.e.*, MAE, R^2 and their corresponding CI). Second, applying different data augmentation techniques (*i.e.*, random shift, mixup in exp. 4, 5) can slightly improve the mentioned metrics and their CI. This is in line with the finding of⁵⁹. Third, many studies have shown the advantages of using age correction techniques. In our case, the implemented technique does not show improvements (exp. 6). However, this technique can enhance the discriminative capacity of BSA for better disease classification (see Section 4.2.1). Finally, using SVR improves our model accuracy over MLP (exp. 7). Overall, each factor contributes to our model accuracy. In the rest of the paper, BSA is computed using 100% data, random shift, mixup, structural age correction techniques, and SVR regressor unless otherwise specified.

TABLE 3 Ablation study for the chronological age estimation. **Red**: best result, **Blue**: second best result. Text or symbols in black: Changes compared to the previous experiment. Text or symbols in gray: No change compared to the previous experiment. The model performance is estimated by different metrics: Mean absolute error (MAE) and the coefficient of determination (R^2). The validation procedure is presented in Section 3.3. We denote MLP, SVR and CI for Multi-layer perceptron, Support Vector Regressor and Confidence Interval. The CI is estimated at 95% confidence level using bootstrapping.

| No. | Data amount | Random Shift | MixUp | Structural Age Correction | Regressor | Young population | | | | Old population | | | |
|-----|-------------|--------------|-------|---------------------------|-----------|------------------|--------------|---------|---------------|----------------|--------------|---------|----------------|
| | | | | | | MAE ▼ | CI | R^2 ▲ | CI | MAE ▼ | CI | R^2 ▲ | CI |
| 1 | 50% | × | × | × | MLP | 4.59 | [4.08, 5.16] | 0.26 | [-0.09, 0.50] | 8.27 | [8.20, 8.35] | -0.84 | [-0.88, -0.80] |
| 2 | 75% | × | × | × | MLP | 3.44 | [3.04, 3.76] | 0.64 | [0.50, 0.74] | 7.72 | [7.60, 7.74] | -0.62 | [-0.69, -0.61] |
| 3 | 100% | × | × | × | MLP | 2.38 | [2.15, 2.59] | 0.85 | [0.80, 0.89] | 4.60 | [4.54, 4.63] | 0.41 | [0.40, 0.43] |
| 4 | 100% | ✓ | × | × | MLP | 2.11 | [1.92, 2.29] | 0.89 | [0.86, 0.92] | 3.98 | [3.92, 3.99] | 0.58 | [0.57, 0.59] |
| 5 | 100% | ✓ | ✓ | × | MLP | 1.92 | [1.75, 2.08] | 0.91 | [0.88, 0.93] | 3.89 | [3.83, 3.90] | 0.60 | [0.60, 0.61] |
| 6 | 100% | ✓ | ✓ | ✓ | MLP | 1.91 | [1.75, 2.08] | 0.91 | [0.88, 0.93] | 3.87 | [3.85, 3.92] | 0.61 | [0.59, 0.61] |
| 7 | 100% | ✓ | ✓ | ✓ | SVR | 1.88 | [1.72, 2.05] | 0.91 | [0.88, 0.93] | 3.83 | [3.80, 3.87] | 0.62 | [0.61, 0.62] |

4.1.2 | Comparison with state-of-the-art methods

In this part, we compare our method with different state-of-the-art methods. For each method below, we used the code available ^{†† ††} and retrained the model using the same data split as in our training process. The first method by Jonsson *et al.* uses a ResNet-like architecture and demonstrated promising results in age prediction²⁴. More recently, Peng *et al.* presented a lightweight architecture named Simple Fully Convolutional Network (SFCN) for this problem⁵⁹. They considered age prediction as a classification problem. To introduce a relationship between close classes, they used a soft label during training. The soft label is a probability distribution centered around the ground-truth age. In another work, Leonardsen *et al.* reused the SFCN backbone and demonstrated that the soft label can lead to better accuracy with in-domain data but the regression version presents a better generalization capacity on out-of-domain data⁶⁰. Table 4 shows the results of the comparison. For the young population, we can remark that our method presents a very low MAE (1.88 years) and very high R^2 (0.91) compared to other state-of-the-art methods. For the older population, all methods present a drop in performance. In this case, our method shows $MAE = 3.83$ years and $R^2 = 0.62$, presenting the best prediction error over all methods. Finally, our method shows better and non-overlapping CI compared to other methods, demonstrating superior performance on chronological age estimation.

4.2 | Disease classification

4.2.1 | Ablation study for binary classification tasks

In this part, we aim at assessing the BSAGE (*i.e.*, the difference between BSA and the chronological subject’s age) feature in the context of specific disease detection (binary classification). To do it, we compare this feature with the brain structure volume feature (denoted as V). We denote $BSAGE_{nc}$ as the BSAGE without age correction (see Section 3.2). Finally, we propose to take advantage of both BSAGE and structure volume biomarker to improve the discriminative capacity of our model.

Table 5 shows the results of the comparison between different features for different classification problems. The balanced accuracy (BACC) is presented. Other metrics are provided in the appendix. First, we can remark that BSAGE (exp. 2, 6) shows better results in BACC and the CI associated than the non corrected version $BSAGE_{nc}$ (exp. 1, 5) in most classification problems (*i.e.*, AD, FTD and MS detection). Only in case of PD detection, the version without age correction shows better results than the

^{††} https://github.com/ha-ha-ha-han/UKBiobank_deep_pretrain

^{†††} <https://github.com/benniatli/BrainAgePredictionResNet>

TABLE 4 Comparison with state-of-the-art methods. **Red**: best result, **Blue**: second best result. The model performance is estimated by different metric: Mean absolute error (MAE) and the coefficient of determination (R^2). For each method, ten cross-validated models were used to predict the chronological age and the 10 outputs were averaged to make the final prediction. We denote CI for Confidence Interval. The CI is estimated at 95% confidence level using bootstrapping. The age for each population is under the form: mean \pm std.

| No. | Method | Young population Age: 14.8 \pm 9.3 | | | | Older population Age: 64.2 \pm 7.9 | | | |
|-----|-------------------------------|---|--------------|------------------------|--------------|---|--------------|------------------------|--------------|
| | | MAE ∇ | CI | R^2 \blacktriangle | CI | MAE ∇ | CI | R^2 \blacktriangle | CI |
| 1 | ResNet-like ²⁴ | 2.84 | [2.53, 3.21] | 0.71 | [0.59, 0.79] | 4.14 | [4.10, 4.18] | 0.54 | [0.53, 0.55] |
| 2 | SFCN soft label ⁵⁹ | 2.78 | [2.52, 3.20] | 0.71 | [0.59, 0.79] | 4.92 | [4.88, 4.97] | 0.32 | [0.35, 0.37] |
| 3 | SFCN regression ⁶⁰ | 2.89 | [2.54, 3.26] | 0.68 | [0.53, 0.78] | 4.60 | [4.56, 4.64] | 0.46 | [0.45, 0.47] |
| 4 | Our method | 1.88 | [1.72, 2.05] | 0.91 | [0.88, 0.93] | 3.83 | [3.80, 3.87] | 0.62 | [0.61, 0.62] |

TABLE 5 Ablation study for binary classification tasks. **Red**: best result, **Blue**: second best result. The balanced accuracy (BACC) is used to assess the model performance (presented in %). We denote BSAGE_{nc}, BSAGE, V and CI for respectively BSAGE with no age correction, BSAGE with age correction, structure volume and Confidence Interval. The CI is estimated at 95% confidence level using bootstrapping. The validation procedure is presented in Section 3.3.

| | No. | Features | AD vs. CN | | FTD vs. CN | | MS vs. CN | | PD vs. CN | | SZ vs. CN | |
|--------------------------------------|-----------|---------------------|--------------|--------------|--------------|--------------|--------------|--------------|--------------|--------------|--------------|--------------|
| | | | BACC | CI | BACC | CI | BACC | CI | BACC | CI | BACC | CI |
| In-domain cross-validation | | | $N = 781$ | | $N = 547$ | | $N = 903$ | | $N = 763$ | | $N = 614$ | |
| | 1 | BSAGE _{nc} | 76.3 | [73.6, 79.1] | 71.4 | [66.8, 75.8] | 70.2 | [67.2, 73.2] | 71.8 | [68.6, 74.9] | 63.9 | [60.0, 67.8] |
| | 2 | BSAGE | 88.2 | [85.9, 90.4] | 86.3 | [82.7, 89.8] | 83.7 | [81.2, 86.1] | 73.5 | [70.4, 76.6] | 77.3 | [73.6, 80.8] |
| | 3 | V | 89.1 | [86.8, 91.3] | 89.4 | [86.1, 92.6] | 79.4 | [76.7, 82.0] | 64.8 | [61.4, 68.1] | 78.2 | [74.6, 81.6] |
| 4 | BSAGE + V | 91.8 | [89.8, 93.6] | 91.3 | [88.2, 94.2] | 84.6 | [82.1, 86.9] | 65.7 | [62.4, 69.0] | 81.0 | [77.5, 84.4] | |
| Out-of-domain independent testset | | | $N = 2103$ | | $N = 1273$ | | $N = 3411$ | | $N = 1360$ | | $N = 1310$ | |
| | 5 | BSAGE _{nc} | 62.3 | [60.4, 64.3] | 63.6 | [56.2, 70.9] | 79.3 | [77.9, 80.6] | 63.3 | [60.3, 66.2] | 73.1 | [67.7, 78.7] |
| | 6 | BSAGE | 78.5 | [76.8, 80.3] | 90.6 | [85.2, 95.2] | 84.3 | [83.1, 85.5] | 52.8 | [48.3, 57.2] | 69.0 | [63.7, 74.5] |
| | 7 | V | 86.3 | [84.8, 87.7] | 90.1 | [84.5, 95.1] | 71.1 | [69.5, 72.7] | 58.3 | [54.0, 62.4] | 76.6 | [71.0, 81.8] |
| 8 | BSAGE + V | 86.0 | [84.4, 87.5] | 91.0 | [85.6, 95.6] | 83.0 | [81.7, 84.3] | 59.8 | [55.6, 64.3] | 83.2 | [78.1, 88.1] | |

corrected version in the out-of-domain dataset. Second, we observe that BSAGE (exp. 2, 6) shows high BACC in FTD detection and MS detection while the results of structure volume shows its effectiveness in AD detection, FTD detection and SZ detection. In other cases (*i.e.*, PD detection), both features moderately perform on in-domain data and poorly perform on out-of-domain data. From this observation, both the BSAGE and the structure volumes demonstrate discriminative power for different disease detection tasks. Thus, it should be beneficial to combine them for a better discriminative capacity. As a result, the combination of BSAGE and structure volume (exp. 4, 8) shows most of the time the best or the second best BACC.

4.2.2 | Multi-disease classification

Table 6 shows the results for the multi-disease classification problem. We estimated the balanced accuracy (BACC), accuracy (ACC) and area under curve (AUC) of our model. We performed classification using the true age (exp. 1, 7) and the predicted subject's age (exp. 2, 8) to confirm that estimating brain age at structure level provides better results than using a global age estimation with real or estimated values. Moreover, these baseline methods enable to estimate the biases present between populations in terms of age. Indeed, there was some bias in age distribution between diseases since for instance the SZ patients were young while compared to the AD patients. Thanks to this analysis, we can observe that BSAGE (exp. 4, 10) and V feature (exp. 5, 11) presents far higher performances and better CIs than the true age and the predicted subject's age. This suggests that

the structure-related information is valuable in classification context. Furthermore, we compared BSAGE with the BrainAGE (*i.e.*, the difference between the predicted subject’s age and the true age) for multi-disease diagnosis (exp. 3, 9). Experimental results suggested that using local brain ages gap estimation (*i.e.*, BSAGE) is more beneficial than the global BrainAGE in multi-disease detection. Besides, although the BSAGE (exp. 4, 10) presents lower performance than the V feature (exp. 5, 11), the two biomarkers can be mutually used to achieve better classification performance. Indeed, their combination (exp. 6, 12) shows the best performance and CI for all proposed metrics. Finally, we included in the Appendix another multi-disease classification performance of CN *vs.* AD *vs.* FTD. This is presented alongside results from state-of-the-art methods, demonstrating the efficiency of our framework in varied diagnostic scenarios.

TABLE 6 Multi-disease classification results. **Red**: best result, **Blue**: second best result. The results are presented in %. We denote BrainAGE for the difference between the predicted age and the true age, BSAGE , V and CI for BSAGE with correction, structure volume and Confidence Interval. The CI is estimated at 95% confidence level using bootstrapping. The validation procedure is presented in Section 3.3.

| | No. | Features | BACC | CI_{BACC} | ACC | CI_{ACC} | AUC | CI_{AUC} |
|--------------------------------------|-----|---------------|-------------|--------------|-------------|--------------|-------------|--------------|
| In-domain cross-validation | 1 | True age | 36.8 | [35.5, 38.0] | 46.4 | [44.3, 48.5] | 76.8 | [75.8, 77.8] |
| | 2 | Predicted age | 33.3 | [31.9, 34.7] | 40.6 | [38.6, 42.7] | 74.7 | [73.2, 75.4] |
| | 3 | BrainAGE | 26.9 | [25.4, 28.4] | 34.4 | [32.3, 36.5] | 66.2 | [63.9, 67.1] |
| | 4 | BSAGE | 58.5 | [56.1, 60.9] | 61.7 | [59.6, 63.9] | 88.0 | [87.0, 89.0] |
| | 5 | V | 64.5 | [62.2, 66.8] | 65.1 | [63.0, 67.2] | 90.2 | [89.3, 91.1] |
| | 6 | BSAGE + V | 68.7 | [66.4, 70.9] | 69.6 | [67.7, 71.6] | 93.2 | [92.4, 93.9] |
| Out-of-domain independent testset | 7 | True age | 34.0 | [32.4, 35.5] | 51.4 | [50.0, 52.8] | 74.3 | [73.0, 75.6] |
| | 8 | Predicted age | 31.7 | [30.4, 33.4] | 41.8 | [40.9, 43.8] | 71.8 | [70.4, 73.1] |
| | 9 | BrainAGE | 27.5 | [26.8, 28.2] | 50.8 | [53.9, 56.7] | 70.5 | [68.9, 72.4] |
| | 10 | BSAGE | 44.7 | [41.6, 48.0] | 57.0 | [55.6, 58.4] | 82.6 | [80.9, 84.3] |
| | 11 | V | 58.7 | [55.4, 61.9] | 59.4 | [58.0, 60.8] | 86.8 | [85.6, 87.9] |
| | 12 | BSAGE + V | 63.3 | [60.1, 66.5] | 66.1 | [64.8, 67.5] | 90.6 | [89.4, 91.8] |

To better confirm the advantages of BSAGE over BrainAGE, we conducted an analysis of their respective confusion matrices using out-of-domain data (independent testset). These matrices are presented in Figure 3. Notably, when employing BSAGE features, the SVM classifier is capable of generating predictions for all classes. Although the precision for certain classes, such as PD and SZ, may not be ideal, it is still better than BrainAGE features, where the SVM fails to generate predictions for the FTD, PD, and SZ classes. Instead, these classes are frequently misclassified as CN, AD, or MS. This misclassification may be attributed to an overlap in the BrainAGE distribution between the (FTD, PD, SZ) and (CN, AD, MS) classes (see Section 4.3).

4.3 | Predicted brain age gap of different populations

In this section, we compare the predicted brain age gap between different populations (*i.e.*, CN, AD, FTD, MS, PD and SZ). Figure 4 summarizes the distribution of predicted brain age gap for six considered populations. The median and mean predicted brain ages of CN, AD, FTD, MS, PD and SZ are respectively (-1.1, -1.0), (3.3, 3.4), (8.3, 9.2), (11.2, 11.8), (1.0, 1.0) and (6.2, 6.1). First, we observe that the CN class has the mean and median closest to 0 as expected. Second, the BrainAGE of all patient groups is significantly higher than the cognitively normal group ($p < 0.0001$ with T-test). Third, PD pathology seems to be closest to healthy people. Indeed, although T1 weighted MRI presents high contrast of grey/white matter, poor contrast may be found in structures related to PD (*e.g.*, subthalamic nuclei)⁶¹. This may explain the proximity of this class with CN class and the poor performance in PD detection (see Table 5). Fourth, the FTD group presents a more advanced aging process than AD group which is in line with the finding of Lee *et al.*⁶². Finally, we found the same magnitude of BSAGE for MS (11.2 years) as Cole *et al.* (about 10.8 years)⁶³, for AD (3.3 years) as Sendi *et al.* (2.1 years)⁶⁴ and for SZ (6.2 years) as Koutsouleris *et al.* (5.5 years)²⁹.

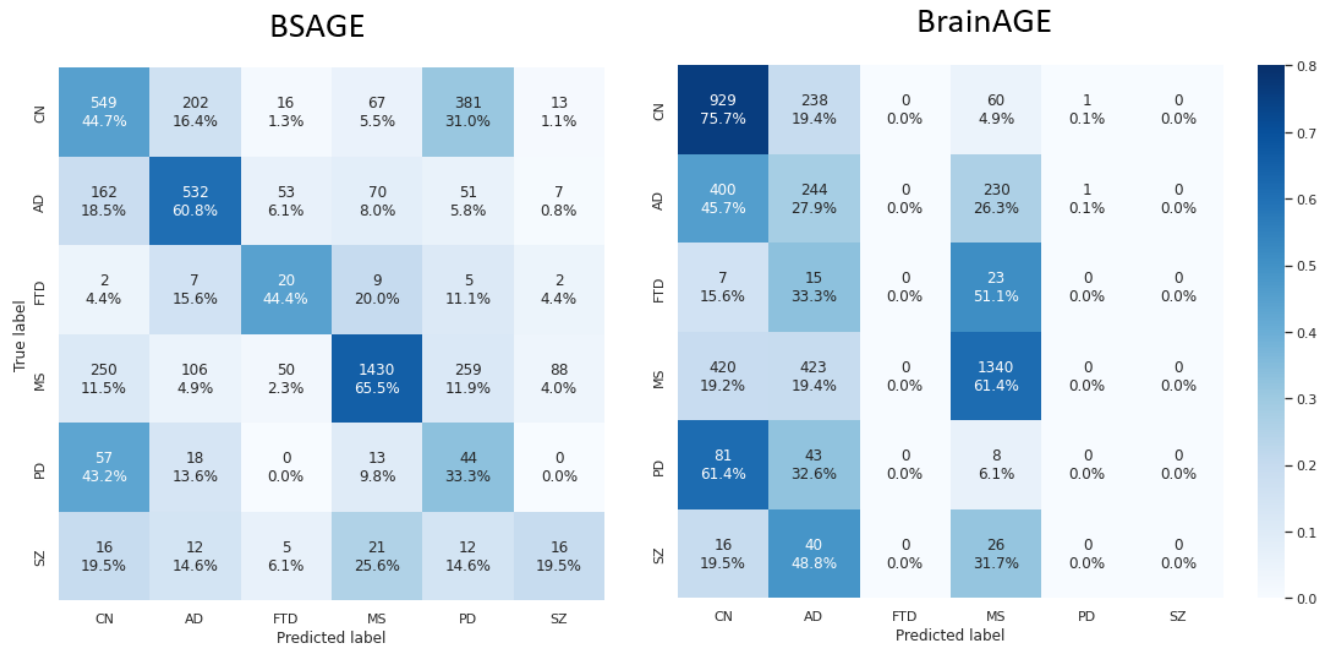


FIGURE 3 Confusion matrix associated with BSAGE features (left) and BrainAGE features (right) computed on out-of-domain data (independent testset).

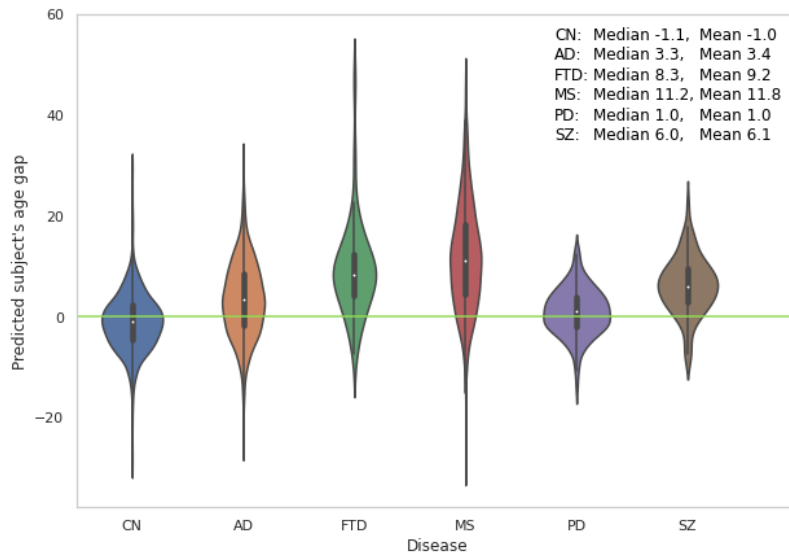


FIGURE 4 Predicted brain age of different populations in out-of-domain data (independent testset). The white point presents the position of the mean value.

4.4 | Interpretation of brain structure age gap estimation

In this section, we propose to visualize the variation of the age gap between brain structures. The presented results in Figure 5 correspond to the average BSAGE value for each structure on different populations of our out-of-domain datasets. We use the same color bar for all populations to compare the impact of each disease on the aging process.

For the AD group, the region surrounding the hippocampus is highlighted as the most accelerated aging area. This region is well-known to be related to AD^{65,66,67,68}. For the FTD group, the accelerated aging pattern is mainly located in the temporal and

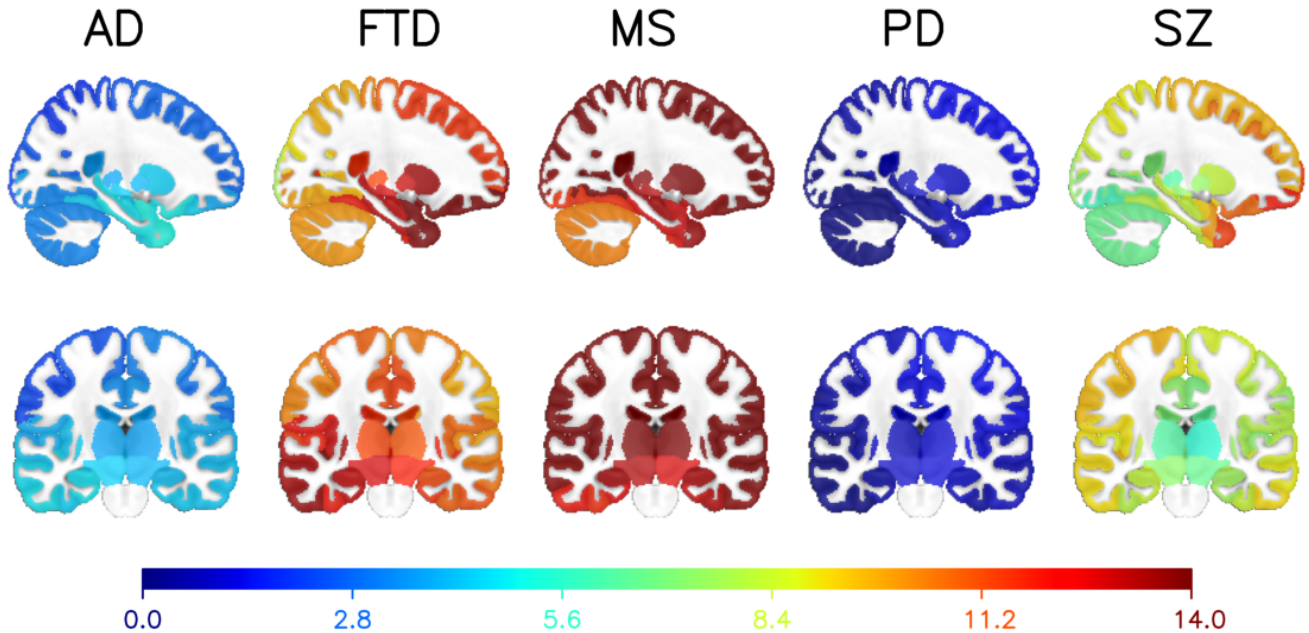


FIGURE 5 BSAGE of different populations in out-of-domain data (independent testset).

frontal lobes which are in line with current literature^{69,70}. For the MS group, the area with the highest accelerated aging pattern is similar to the finding of Cortese *et al.* (*i.e.*, thalamus and global cortical grey matter)⁷¹. For the PD group, all regions seem to be close to healthy people as discussed in Section 4.3. Finally, for the SZ group, the prefrontal and medial temporal lobe regions are highlighted which is coherent with several studies^{72,73}.

We further analyzed the brain structures showing the most significant age differences for each disease, as outlined in Table 7. Firstly, many of the brain structures we previously mentioned also appear on this list, which is consistent with our expectations. Secondly, there's a variation in the ranking of brain structures based on their mean age differences across diseases. This distinction highlights the reason our BSAGE features are more insightful than the overall brain age gap (BrainAGE) for multi-disease diagnosis.

5 | DISCUSSION

In this work, we proposed an approach to estimate brain age at structure level. We showed that this feature can be used for different purposes. First, it can be directly used to accurately estimate the chronological age. Second, this can be used to compute the BSAGE (*i.e.*, the difference between brain structure ages and the chronological age). This biomarker presents discriminative patterns which are useful for the multi-disease classification problem (*i.e.*, CN vs. AD vs. FTD vs. MS vs. PD vs. SZ).

For the problem of chronological age estimation, we observed that the model accuracy was heavily influenced by different factors: data amount and data augmentation techniques. In our experiments, the model accuracy was consistently improved when the data amount was increased and we did not observe saturation. This suggests that training our framework on more data could yield higher accuracy. In this study, due to the limited training data, we instead applied several data augmentation techniques to improve the generalization capacity of our model. Experimental results showed that the random shift and mixup techniques have a huge impact on our model performance (see Table 3). Moreover, the resulting BSA can enable a more accurate subject's age prediction. While our framework was training over a large range of ages (*i.e.*, 0 to 95 years old), it achieved higher accuracy when predicting on young population (*i.e.*, ABIDE dataset $MAE = 1.88$ years) than on older population (*i.e.*, UKBioBank dataset $MAE = 3.83$ years). Our approach outperformed other state-of-the-art methods with 1.20 years MAE lower on the young population and 0.99 year MAE lower on the old population. When evaluating our approach on different disease populations (*i.e.*, AD, FTD, MS, PD, SZ), our findings were in line with current knowledge in the literature (see Section 4.3 for more details).

TABLE 7 Ten brain structures with highest age gap for each disease. We denote L. for Left, R. for Right. The full table is provided in Appendix.

| AD | | FTD | | MS | |
|----------------------------|--------------|----------------------------|--------------|-------------------------------------|--------------|
| Structure | Mean age gap | Structure | Mean age gap | Structure | Mean age gap |
| L. Temporal Pole | 5.23 | L. Temporal Pole | 16.11 | L. Superior Occipital Gyrus | 16.59 |
| L. Amygdala | 5.20 | L. Medial Orbital Gyrus | 15.62 | L. Cuneus | 16.55 |
| L. Posterior Orbital Gyrus | 5.13 | L. Gyrus Rectus | 15.49 | L. Precuneus | 16.42 |
| L. Entorhinal Area | 5.05 | L. Posterior Orbital Gyrus | 15.42 | R. Superior Occipital Gyrus | 16.37 |
| L. Parahippocampal Gyrus | 4.98 | R. Gyrus Rectus | 15.21 | R. Postcentral Gyrus Medial Segment | 16.33 |
| L. Planum Polare | 4.97 | L. Entorhinal Area | 15.03 | R. Superior Frontal Gyrus | 16.23 |
| L. Inferior Temporal Gyrus | 4.96 | L. Anterior Orbital Gyrus | 14.94 | R. Supplementary Motor Cortex | 16.23 |
| L. Hippocampus | 4.90 | R. Anterior Orbital Gyrus | 14.76 | L. Supplementary Motor Cortex | 16.22 |
| L. Anterior Insula | 4.89 | R. Medial Orbital Gyrus | 14.71 | R. Supramarginal Gyrus | 16.19 |
| L. Basal Forebrain | 4.88 | L. Medial Frontal Cortex | 14.68 | R. Cuneus | 16.18 |

| PD | | SZ | |
|---|--------------|--------------------------------------|--------------|
| Structure | Mean age gap | Structure | Mean age gap |
| R. Lateral Orbital Gyrus | 2.58 | L. Lateral Orbital Gyrus | 13.09 |
| R. Frontal Pole | 2.56 | L. Anterior Orbital Gyrus | 12.46 |
| R. Anterior Orbital Gyrus | 2.39 | L. Temporal Pole | 11.97 |
| R. Orbital of Inferior Frontal Gyrus | 2.25 | L. Frontal Pole | 11.79 |
| R. Medial Orbital Gyrus | 2.24 | L. Orbital of Inferior Frontal Gyrus | 11.55 |
| R. Middle Frontal Gyrus | 2.17 | L. Gyrus Rectus | 11.40 |
| R. Triangular of Inferior Frontal Gyrus | 2.15 | L. Posterior Orbital Gyrus | 11.29 |
| R. Superior Frontal Gyrus | 2.15 | R. Frontal Pole | 11.26 |
| R. Medial Frontal Cortex | 2.06 | L. Medial Orbital Gyrus | 11.13 |
| R. Gyrus Rectus | 1.97 | R. Anterior Orbital Gyrus | 11.13 |

Finally, we observed that the predicted age distributions are different between diseases, suggesting a discriminative power of our BSA feature.

While most papers used the global BrainAGE to show that a disease can present an accelerated or delayed aging process on a population^{28,29,19}, only a few approaches have proposed to use it for classification^{30,31,32,33}. Moreover, these studies dedicated to classification had a common limitation. Indeed, it might exist a range of global BrainAGE values that is presented in different populations. In our case, all populations had global BrainAGE values in range [-5, 10] (see Figure 4). When the number of classes is increased, this limitation becomes more challenging. This might explain why existing BrainAGE-based algorithms only address classification problems with a low number of class (*e.g.*, binary classification). This raises the need for other features better describing the brain aging process for classification. Thus, we propose to extend the notion of BrainAGE to BSAGE. This local feature offers a richer representation of the brain aging process than global BrainAGE estimation. Consequently, this information is important for improving the multi-disease classification as analyzed in Section 4.4.

In addition to improve classification performance, BSAGE can be projected into a brain segmentation for visualization purpose. Principal remarks for each population were discussed in Section 4.4. Overall, it gives some insights about the specific structures impacted by each disease. The main patterns of each disease highlighted by our color maps are coherent with current literature (as discussed in Section 4.4). This presents an important clinical value of our framework in a real medical context.

Based on brain age prediction, several methods have been developed that can potentially identify brain regions affected by diseases. For example, Levakov *et al.* proposed using Explainable AI maps of CNNs to emphasize brain regions that significantly contribute to brain age prediction⁷⁴. Hypothetically, if such techniques were applied to populations with brain disorders, they might uncover regions associated with signs of either accelerated or delayed brain aging due to the disorder. In our method, the BSAGE maps exhibit other interesting properties. Specifically, our BSAGE maps offer a quantitative measure that captures the abnormality of brain structure at the subject level. In contrast, explanation maps present a more qualitative insight into the relative significance of each feature during the decision-making phase. For instance, within an explanation map of an AD patient, it remains uncertain whether the non-emphasized regions (areas the models did not consider important for their decision) are in a healthy state or just non-informative (either redundant with other structures, or possibly too noisy across subjects, etc.). Additionally, explanation maps typically normalize values within a same range of values, making any comparison between two maps purely qualitative.

One limitation of our study is the lack of an independent in-domain testset for evaluating multi-disease classification. Typically, leveraging a separate in-domain testset would enable a more rigorous analysis of performance differences between in-domain

and out-of-domain settings. In our case, however, the use of a small testset could compromise the representativeness of the data, affecting the reliability of performance estimates. Conversely, using a large portion of the data for testing could reduce the amount of data available for effective model training. To balance these competing needs, we proposed to use a cross-validation strategy. While this approach offers a reasonable compromise between performance estimation and training robustness, it admittedly limits our ability to investigate performance disparities between in-domain and out-of-domain scenarios explicitly.

Finally, some diseases such as Parkinson's Disease cannot be easily detected using T1 weighted MRI. Future works should focus on the multi-modal input to either accurately estimate brain age or produce a more discriminative BSAGE feature. In addition, we use the same CNN architecture to analyze different brain locations. This can be not optimal due to the fact that different brain locations may have a specific set of patterns. An auto-search algorithm to select an optimal architecture for each brain region would be beneficial for further analysis.

6 | CONCLUSION

In this paper, we propose to extend the notion of brain age by estimating the brain age at voxel level. This voxelwise brain age map is then used to compute BSA. This biomarker can be used for different purposes. First, it can be used to predict the chronological age of people. The deviation of the predicted age from the subject's age can provide insight about the individual brain status. Second, by subtracting the subject's age from the BSA, we obtain a BSA gap estimation (*i.e.*, BSAGE). This feature can be mutually used with other biomarkers such as structure volume for disease detection. Finally, this feature can be also visualized to detect brain abnormality in MRI. Such a tool can help clinicians in making more informed decisions.

ACKNOWLEDGMENTS

This work benefited from the support of the project DeepvolBrain of the French National Research Agency (ANR-18-CE45-0013). This study was achieved within the context of the Laboratory of Excellence TRAIL ANR-10-LABX-57 for the BigDataBrain project. Moreover, we thank the Investments for the future Program IdEx Bordeaux (ANR-10-IDEX-03-02 and RRI "IMPACT"), the French Ministry of Education and Research, and the CNRS for DeepMultiBrain project.

The ADNI data used in the preparation of this manuscript were obtained from the Alzheimer's Disease Neuroimaging Initiative (ADNI) (National Institutes of Health Grant U01 AG024904). The ADNI is funded by the National Institute on Aging and the National Institute of Biomedical Imaging and Bioengineering and through generous contributions from private partners as well as nonprofit partners listed at: <https://ida.loni.usc.edu/collaboration/access/appLicense.jsp>. Private sector contributions to the ADNI are facilitated by the Foundation for the National Institutes of Health (www.fnih.org). The grantee organization is the Northern California Institute for Research and Education, and the study was coordinated by the Alzheimer's Disease Cooperative Study at the University of California, San Diego. ADNI data are disseminated by the Laboratory for NeuroImaging at the University of California, Los Angeles. This research was also supported by NIH grants P30AG010129, K01 AG030514 and the Dana Foundation.

The NDAR data used in the preparation of this manuscript were obtained from the NIH-supported National Database for Autism Research (NDAR). This is supported by the National Institute of Child Health and Human Development, the National Institute on Drug Abuse, the National Institute of Mental Health, and the National Institute of Neurological Disorders and Stroke. A listing of the participating sites and a complete listing of the study investigators can be found at http://pediatricmri.nih.gov/nihpd/info/participating_centers.html.

The ICBM data used in the preparation of this manuscript were supported by Human Brain Project grant PO1MHO52176-11 and Canadian Institutes of Health Research grant MOP- 34996.

The IXI data used in the preparation of this manuscript were supported by the U.K. Engineering and Physical Sciences Research Council (EPSRC) GR/S21533/02 - <http://www.brain-development.org/>.

The ABIDE data used in the preparation of this manuscript were supported by ABIDE funding resources listed at http://fcon_1000.projects.nitrc.org/indi/abide/.

The AIBL data used in the preparation of this manuscript were obtained from the AIBL study of ageing funded by the Commonwealth Scientific Industrial Research Organization (CSIRO; a publicly funded government research organization), Science Industry Endowment Fund, National Health and Medical Research Council of Australia (project grant 1011689), Alzheimer's Association, Alzheimer's Drug Discovery Foundation, and an anonymous foundation. See www.aibl.csiro.au for further details.

The ADHAD, DLBS and SALD data used in the preparation of this article were obtained from http://fcon_1000.projects.nitrc.org (Mennes M et al., NeuroImage, 2013; Wei D et al., bioRxiv 2017).

Data used in the preparation of this article were also obtained from the MIRIAD database (Malone IB et al., *NeuroImage*, 2012). The MIRIAD investigators did not participate in analysis or writing of this report. The MIRIAD dataset is made available through the support of the UK Alzheimer's Society (Grant RF116). The original data collection was funded through an unrestricted educational grant from GlaxoSmithKline (Grant 6GKC).

Data used in the preparation of this article were obtained from the Parkinson's Progression Markers Initiative (PPMI) database (www.ppmi-info.org). PPMI – a public-private partnership – was funded by The Michael J. Fox Foundation for Parkinson's Research and funding partners that can be found at <https://www.ppmi-info.org/about-ppmi/who-we-are/study-sponsor>

Data collection and sharing for this project was provided by the Cambridge Centre for Ageing and Neuroscience (CamCAN, <https://camcan-archive.mrc-cbu.cam.ac.uk/dataaccess/>). CamCAN funding was provided by the UK Biotechnology and Biological Sciences Research Council (grant number BB/H008217/1), together with support from the UK Medical Research Council and University of Cambridge, UK.

Data used in the preparation of this work were obtained from the DecNef Project Brain Data Repository (<https://bicer-resource.atr.jp/srpbopen/>) gathered by a consortium as Of Japanese Strategic Research Program for the Promotion of Brain Science (SRPBS) supported by the Japanese Advanced Research and Development Programs for Medical Innovation (AMED, Tanaka SC et al., *Scientific data*, 2021).

TLDNI was funded through the National Institute of Aging, and started in 2010. The primary goals of FTLTLDNI were to identify neuroimaging modalities and methods of analysis for tracking frontotemporal lobar degeneration (FTLD) and to assess the value of imaging versus other biomarkers in diagnostic roles. The Principal Investigator of NIFD was Dr. Howard Rosen, MD at the University of California, San Francisco. The data are the result of collaborative efforts at three sites in North America. For up-to-date information on participation and protocol, please visit <http://memory.ucsf.edu/research/studies/nifd>. Data collection and sharing for this project was funded by the Frontotemporal Lobar Degeneration Neuroimaging Initiative (National Institutes of Health Grant R01 AG032306). The study is coordinated through the University of California, San Francisco, Memory and Aging Center. FTLTLDNI data are disseminated by the Laboratory for Neuro Imaging at the University of Southern California.

The C-MIND data used in the preparation of this article were obtained from the C-MIND Data Repository (accessed in Feb 2015) created by the C-MIND study of Normal Brain Development. This is a multisite, longitudinal study of typically developing children from ages newborn through young adulthood conducted by Cincinnati Children's Hospital Medical Center and UCLA and supported by the National Institute of Child Health and Human Development (Contract #s HHSN275200900018C). A listing of the participating sites and a complete listing of the study investigators can be found at <https://research.cchmc.org/c-mind>. The NDAR data used in the preparation of this manuscript were obtained from the NIH-supported National Database for Autism Research (NDAR). NDAR is a collaborative informatics system created by the National Institutes of Health to provide a national resource to support and accelerate research in autism. The NDAR dataset includes data from the NIH Pediatric MRI Data Repository created by the NIH MRI Study of Normal Brain Development. This is a multisite, longitudinal study of typically developing children from ages newborn through young adulthood conducted by the Brain Development Cooperative Group and supported by the National Institute of Child Health and Human Development, the National Institute on Drug Abuse, the National Institute of Mental Health, and the National Institute of Neurological Disorders and Stroke (Contract #s N01-HD02-3343, N01-MH9-0002, and N01-NS-9-2314, -2315, -2316, -2317, -2319 and -2320). A listing of the participating sites and a complete listing of the study investigators can be found at http://pediatricmri.nih.gov/nihpd/info/participating_centers.html.

The NACC database was funded by NIA/NIH Grants listed at <https://naccddata.org/publish-project/authors-checklist#acknowledgment>.

This research has been conducted using data from UK Biobank, a major biomedical database. . See <https://www.ukbiobank.ac.uk/> for further details.

Data collection has been supported by a grant provided by the French State and handled by the "Agence Nationale de la Recherche," within the framework of the "Investments for the Future" programme, under the reference ANR-10-COHO-002, Observatoire Français de la Sclérose en Plaques (OFSEP) & "Eugène Devic EDMUS Foundation against multiple sclerosis".

Data was downloaded from the COllaborative Informatics and Neuroimaging Suite Data Exchange tool (COINS; <http://coins.mrn.org/dx>) and data collection was funded by NIMH R01MH084898-01A1, "Brain Glutamate and Outcome in Schizophrenia", PI: J. Bustillo.

Data were provided in part by OASIS : OASIS-1: Cross-Sectional: Principal Investigators: D. Marcus, R. Buckner, J. Csernansky J. Morris; P50 AG05681, P01 AG03991, P01 AG026276, R01 AG021910, P20 MH071616, U24 RR021382

FINANCIAL DISCLOSURE

None reported.

CONFLICT OF INTEREST

The authors declare no potential conflict of interests.

REFERENCES

1. Franke K, Gaser C. Ten Years of BrainAGE as a Neuroimaging Biomarker of Brain Aging: What Insights Have We Gained?. *Frontiers in Neurology*. 2019;10:789.
2. Chang CH, Lin CS, Luo YS, Lee YT, Lin C. Electrocardiogram-Based Heart Age Estimation by a Deep Learning Model Provides More Information on the Incidence of Cardiovascular Disorders. *Frontiers in Cardiovascular Medicine*. 2022;9:754909.
3. Raghu VK, Weiss J, Hoffmann U, Aerts HJWL, Lu MT. Deep Learning to Estimate Biological Age From Chest Radiographs. *JACC: Cardiovascular Imaging*. 2021;14:2226–2236.
4. Nakamura E, Miyao K. A Method for Identifying Biomarkers of Aging and Constructing an Index of Biological Age in Humans. *The Journals of Gerontology Series A: Biological Sciences and Medical Sciences*. 2007;62:1096–1105.
5. Chen BH, Marioni RE, Colicino E, et al. DNA methylation-based measures of biological age: meta-analysis predicting time to death. *Aging*. 2016;8:1844–1865.
6. Ignjatovic V, Lai C, Summerhayes R, et al. Age-Related Differences in Plasma Proteins: How Plasma Proteins Change from Neonates to Adults. *PLoS ONE*. 2011;6:17213.
7. Armanious K, Abdulatif S, Shi W, et al. Age-Net: An MRI-Based Iterative Framework for Brain Biological Age Estimation. *IEEE Transactions on Medical Imaging*. 2021;40:1778–1791.
8. Tian YE, Cropley V, Maier AB, Lautenschlager NT, Breakspear M, Zalesky A. Heterogeneous aging across multiple organ systems and prediction of chronic disease and mortality. *medRxiv*. 2023. doi: 10.1101/2022.09.03.22279337
9. Le Goallec A, Diai S, Collin Sea. Using deep learning to predict abdominal age from liver and pancreas magnetic resonance images. *Nature Communications*. 2022;13:1979. doi: 10.1038/s41467-022-29525-9
10. Mauer MA, Well EJ, Herrmann J, et al. Automated age estimation of young individuals based on 3D knee MRI using deep learning. *International Journal of Legal Medicine*. 2021;135(2):649–663. doi: 10.1007/s00414-020-02465-z
11. Peters R. Aging and the brain. *Postgraduate Medical Journal*. 2006;82:84–88.
12. Huizinga W, Poot DHJ, Vernooij MW, et al. A spatio-temporal reference model of the aging brain. *NeuroImage*. 2018;169:11–22.
13. Jia X, Liang P, Li Y, Shi L, Wang D, Li K. Longitudinal Study of Gray Matter Changes in Parkinson Disease. *American Journal of Neuroradiology*. 2015;36:2219–2226.
14. Tisserand DJ, Boxel vMPJ, Pruessner JC, Hofman P, Evans AC, Jolles J. A Voxel-based Morphometric Study to Determine Individual Differences in Gray Matter Density Associated with Age and Cognitive Change Over Time. *Cerebral Cortex*. 2004;14:966–973.
15. Coupé P, Manjón JV, Lanuza E, Catheline G. Lifespan Changes of the Human Brain In Alzheimer's Disease. *Scientific Reports*. 2019;9:3998.
16. Coupé P, Manjón JV, Mansencal B, Tourdias T, Catheline G, Planche V. Hippocampal-amygdalo-ventricular atrophy score: Alzheimer disease detection using normative and pathological lifespan models. *Human Brain Mapping*. 2022;43:3270–3282.
17. Cole JH, Franke K. Predicting Age Using Neuroimaging: Innovative Brain aging Biomarkers. *Trends in Neurosciences*. 2017;40:681–690.
18. Mishra S, Beheshti I, Khanna P. A Review of Neuroimaging-driven Brain Age Estimation for identification of Brain Disorders and Health Conditions. *IEEE Reviews in Biomedical Engineering*. 2021:1–1.
19. Franke K, Ziegler G, Klöppel S, Gaser C. Estimating the age of healthy subjects from T1-weighted MRI scans using kernel methods: Exploring the influence of various parameters. *NeuroImage*. 2010;50:883–892.
20. Liem F, Varoquaux G, Kynast J, et al. Predicting brain-age from multimodal imaging data captures cognitive impairment. *NeuroImage*. 2017;148:179–188.
21. Cole JH, Ritchie SJ, Bastin ME, et al. Brain age predicts mortality. *Molecular Psychiatry*. 2018;23:1385–1392.
22. Binti KM, Baltatzis V, Kolbeinsson A, Hammers A, Rueckert D. Patch-based brain age estimation from mr images. In: , Springer, 2020:98–107.
23. Cole JH, Poudel RPK, Tsagkrasoulis D, et al. Predicting brain age with deep learning from raw imaging data results in a reliable and heritable biomarker. *NeuroImage*. 2017;163:115–124.
24. Jonsson BA, Bjornsdottir G, Thorgerisson TE, et al. Brain age prediction using deep learning uncovers associated sequence variants. *Nature Communications*. 2019;10:5409.
25. Bermudez C, Plassard AJ, Chaganti S, et al. Anatomical context improves deep learning on the brain age estimation task. *Magnetic Resonance Imaging*. 2019;62:70–77.
26. Ueda M, Ito K, Wu K, et al. An Age Estimation Method Using 3D-CNN From Brain MRI Images. In: IEEE. 2019:380–383.
27. Binti KM, Baltatzis V, Kolbeinsson A, Hammers A, Rueckert D. Patch-Based Brain Age Estimation from MR Images. In: , , 12449. , 2020:98–107.
28. Franke K, Luders E, May A, Wilke M, Gaser C. Brain maturation: Predicting individual BrainAGE in children and adolescents using structural MRI. *NeuroImage*. 2012;63:1305–1312.
29. Koutsouleris N, Davatzikos C, Borgwardt S, et al. Accelerated Brain Aging in Schizophrenia and Beyond: A Neuroanatomical Marker of Psychiatric Disorders. *Schizophrenia Bulletin*. 2014;40:1140–1153.
30. Gaser C, Franke K, Klöppel S, Koutsouleris N, Sauer H. BrainAGE in Mild Cognitive Impaired Patients: Predicting the Conversion to Alzheimer's Disease. *PLoS ONE*. 2013;8:67346.
31. Franke K, Gaser C. Dementia classification based on brain age estimation. In: aws. 2014:48–54.
32. Varzandian A, Razo MAS, Sanders MR, Atmakuru A, Fatta GD. Classification-Biased Apparent Brain Age for the Prediction of Alzheimer's Disease. *Frontiers in Neuroscience*. 2021;15:673120.
33. Cheng J, Liu Z, Guan H, et al. Brain Age Estimation From MRI Using Cascade Networks With Ranking Loss. *IEEE Transactions on Medical Imaging*. 2021;40:3400–3412.
34. Beheshti I, Gravel P, Potvin O, Dieumegarde L, Duchesne S. A novel patch-based procedure for estimating brain age across adulthood. *NeuroImage*. 2019;197:618–624. doi: 10.1016/j.neuroimage.2019.05.025
35. Popescu SG, Glocker B, Sharp DJ, Cole JH. Local Brain-Age: A U-Net Model. *Frontiers in Aging Neuroscience*. 2021;13:761954. doi: 10.3389/fnagi.2021.761954

36. Martino AD, Yan CG, Li Q, et al. The autism brain imaging data exchange: towards a large-scale evaluation of the intrinsic brain architecture in autism. *Molecular Psychiatry*. 2014;19:659–667.
37. Martino AD, O'Connor D, Chen B, et al. Enhancing studies of the connectome in autism using the autism brain imaging data exchange II. *Scientific Data*. 2017;4:170010.
38. Jr CRJ, Bernstein MA, Fox NC, et al. The Alzheimer's disease neuroimaging initiative (ADNI): MRI methods. *Journal of Magnetic Resonance Imaging*. 2008;27:685–691.
39. Ellis KA, Bush AI, Darby D, et al. The Australian Imaging, Biomarkers and Lifestyle (AIBL) study of aging: methodology and baseline characteristics of 1112 individuals recruited for a longitudinal study of Alzheimer's disease. *International Psychogeriatrics*. 2009;21:672–687.
40. Mazziotta J, Toga A, Evans A, et al. A Probabilistic Atlas and Reference System for the Human Brain: International Consortium for Brain Mapping (ICBM). *Philosophical Transactions: Biological Sciences*. 2001;356:1293–1322.
41. Payakachat N, Tilford JM, Ungar WJ. National Database for Autism Research (NDAR): Big Data Opportunities for Health Services Research and Health Technology Assessment. *PharmacoEconomics*. 2016;34:127–138.
42. LaMontagne PJ, Benzinger TL, Morris JC, et al. OASIS-3: Longitudinal Neuroimaging, Clinical, and Cognitive Dataset for Normal Aging and Alzheimer Disease. *medrxiv*. 2019. doi: 10.1101/2019.12.13.19014902
43. Bycroft C, Freeman C, Petkova D, et al. The UK Biobank resource with deep phenotyping and genomic data. *Nature*. 2018;562:203–209.
44. Tanaka SC, Yamashita A, Yahata N, et al. A multi-site, multi-disorder resting-state magnetic resonance image database. *Scientific Data*. 2021;8:227.
45. Taylor JR, Williams N, Cusack R, et al. The Cambridge Centre for aging and Neuroscience (Cam-CAN) data repository: Structural and functional MRI, MEG, and cognitive data from a cross-sectional adult lifespan sample. *NeuroImage*. 2017;144:262–269.
46. Parkinson Progression Marker Initiative . The Parkinson Progression Marker Initiative (PPMI). *Progress in Neurobiology*. 2011;95:629–635.
47. Vukusic S, Casey R, Rollot F, et al. Observatoire Français de la Sclérose en Plaques (OFSEP): A unique multimodal nationwide MS registry in France. *Multiple Sclerosis Journal*. 2020;26:118–122.
48. Beekly DL, Ramos EM, Lee WW, et al. The National Alzheimer's Coordinating Center (NACC) Database: The Uniform Data Set. *Alzheimer Disease & Associated Disorders*. 2007;21:249–258.
49. Malone IB, Cash D, Ridgway GR, et al. MIRIAD—Public release of a multiple time point Alzheimer's MR imaging dataset. *NeuroImage*. 2013;70:33–36.
50. Bustillo JR, Jones T, Chen H, et al. Glutamatergic and Neuronal Dysfunction in Gray and White Matter: A Spectroscopic Imaging Study in a Large Schizophrenia Sample. *Schizophrenia Bulletin*. 2016:122.
51. Manjón JV, Coupé P, Martí-Bonmati L, Collins DL, Robles M. Adaptive non-local means denoising of MR images with spatially varying noise levels: Spatially Adaptive Nonlocal Denoising. *Journal of Magnetic Resonance Imaging*. 2010;31:192–203.
52. Tustison NJ, Avants BB, Cook PA, et al. N4ITK: Improved N3 Bias Correction. *IEEE Transactions on Medical Imaging*. 2010;29:1310–1320.
53. Avants BB, Tustison NJ, Song G, Cook PA, Klein A, Gee JC. A reproducible evaluation of ANTs similarity metric performance in brain image registration. *NeuroImage*. 2011;54:2033–2044.
54. Manjón JV, Tohka J, García-Martí G, et al. Robust MRI brain tissue parameter estimation by multistage outlier rejection. *Magnetic Resonance in Medicine*. 2008;59:866–873.
55. Manjón JV, Eskildsen SF, Coupé P, Romero JE, Collins DL, Robles M. Nonlocal Intracranial Cavity Extraction. *International Journal of Biomedical Imaging*. 2014;2014:1–11.
56. Coupé P, Mansencal B, Clément M, et al. AssemblyNet: A large ensemble of CNNs for 3D whole brain MRI segmentation. *NeuroImage*. 2020;219:117026.
57. Zhang H, Cisse M, Dauphin YN, Lopez-Paz D. mixup: Beyond Empirical Risk Minimization. *arXiv:1710.09412 [cs, stat]*. 2018.
58. Smith SM, Vidaurde D, Alfaro-Almagro F, Nichols TE, Miller KL. Estimation of brain age delta from brain imaging. *NeuroImage*. 2019;200:528–539.
59. Peng H, Gong W, Beckmann CF, Vedaldi A, Smith SM. Accurate brain age prediction with lightweight deep neural networks. *Medical Image Analysis*. 2021;68:101871.
60. Leonardsen EH, Peng H, Kaufmann T, et al. Deep neural networks learn general and clinically relevant representations of the aging brain. *NeuroImage*. 2022;256:119210.
61. Mortezaazadeh T, Seyedarabi H, Mahmoudian B, Islamian JP. Imaging modalities in differential diagnosis of Parkinson's disease: opportunities and challenges. *Egyptian Journal of Radiology and Nuclear Medicine*. 2021;52:79.
62. Lee J, Burkett BJ, Min HK, et al. Deep learning-based brain age prediction in normal aging and dementia. *Nature Aging*. 2022;2:412–424.
63. Cole JH, Raffel J, Friede T, et al. Longitudinal Assessment of Multiple Sclerosis with the Brain-Age Paradigm. *Annals of Neurology*. 2020;88:93–105.
64. Sendi MS, Salat DH, Calhoun VD. Brain age acceleration as biomarker of Alzheimer's disease progression: Functional network connectivity analysis. *Alzheimer's & Dementia*. 2021;17.
65. Frisoni GB, Fox NC, Jr CRJ, Scheltens P, Thompson PM. The clinical use of structural MRI in Alzheimer disease. *Nature Reviews Neurology*. 2010;6:67–77.
66. Mu Y, Gage FH. Adult hippocampal neurogenesis and its role in Alzheimer's disease. *Molecular Neurodegeneration*. 2011;6:85.
67. Jin K, Peel AL, Mao XO, et al. Increased hippocampal neurogenesis in Alzheimer's disease. *Proceedings of the National Academy of Sciences*. 2004;101:343–347.
68. Hyman BT, Hoesen GWV, Damasio AR, Barnes CL. Alzheimer's Disease: Cell-Specific Pathology Isolates the Hippocampal Formation. *Science*. 1984;225:1168–1170.
69. Whitwell JL, Przybelski SA, Weigand SD, et al. Distinct anatomical subtypes of the behavioural variant of frontotemporal dementia: a cluster analysis study. *Brain*. 2009;132:2932–2946.
70. Boeve BF, Boxer AL, Kumfor F, Pijnenburg Y, Rohrer JD. Advances and controversies in frontotemporal dementia: diagnosis, biomarkers, and therapeutic considerations. *The Lancet Neurology*. 2022;21:258–272.
71. Cortese R, Collorone S, Ciccarelli O, Toosy AT. Advances in brain imaging in multiple sclerosis. *Therapeutic Advances in Neurological Disorders*. 2019;12:175628641985972.
72. Karlsgodt KH, Sun D, Cannon TD. Structural and Functional Brain Abnormalities in Schizophrenia. *Current Directions in Psychological Science*. 2010;19:226–231.

73. DeLisi LE, Szulc KU, Bertisch HC, Majcher M, Brown K. Understanding structural brain changes in schizophrenia. *Dialogues in Clinical Neuroscience*. 2006;8:71–78.
74. Levakov G, Rosenthal G, Shelef I, Raviv TR, Avidan G. From a deep learning model back to the brain-Identifying regional predictors and their relation to aging. *Human Brain Mapping*. 2020;41(12):3235–3252. doi: 10.1002/hbm.25011
75. Nguyen HD, Clément M, Planche V, Mansencal B, Coupé P. Deep grading for MRI-based differential diagnosis of Alzheimer’s disease and Frontotemporal dementia. *Artificial Intelligence in Medicine*. 2023;144:102636.

Appendix

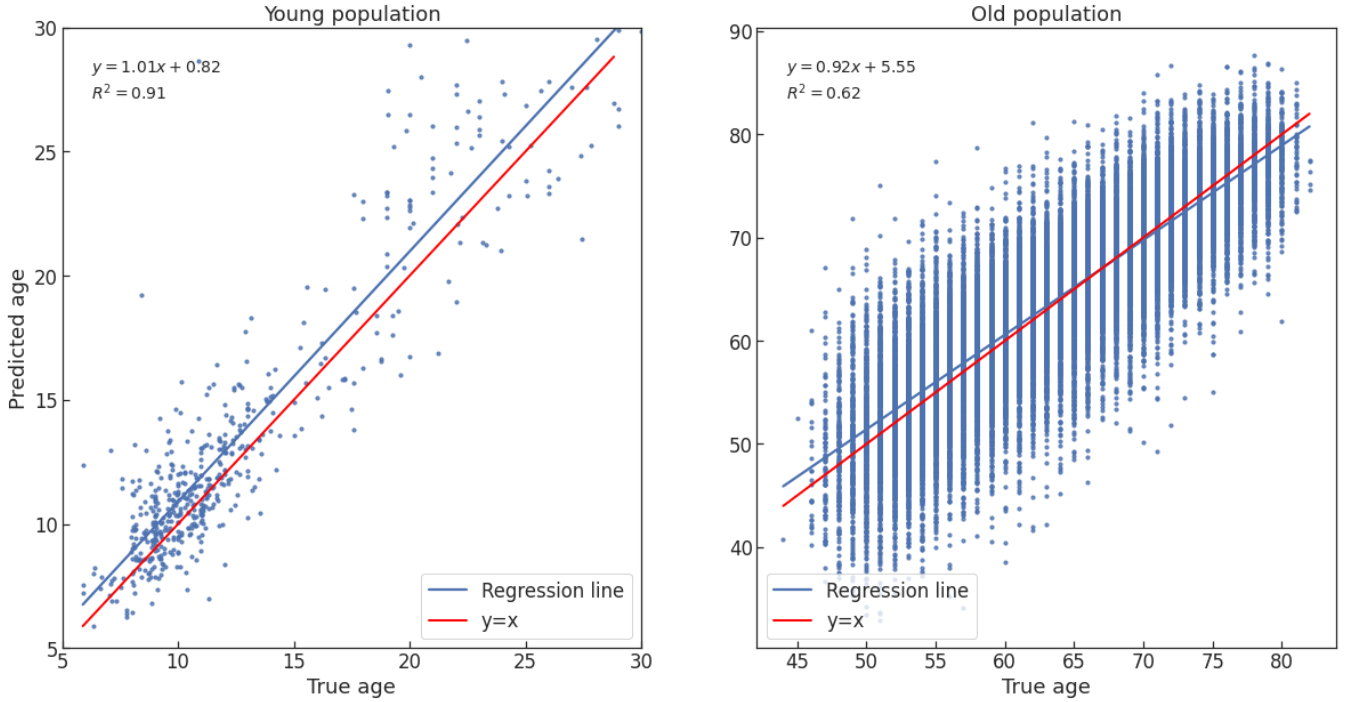


FIGURE A1 Our regression lines in young and old population.

TABLE A1: Ablation study for binary classification tasks. **Red**: best result, **Blue**: second best result. The accuracy (ACC) is used to assess the model performance (presented in %). We denote $BSAGE_{nc}$, $BSAGE$ and V for respectively $BSAGE$ with no age correction, $BSAGE$ with age correction and structure volume. The validation procedure is presented in Section 3.3.

| | No. | Features | AD vs. CN | FTD vs. CN | MS vs. CN | PD vs. CN | SZ vs. CN |
|--------------------------------------|-----|--------------|------------|------------|------------|------------|------------|
| In-domain cross-validation | | | $N = 781$ | $N = 547$ | $N = 903$ | $N = 763$ | $N = 614$ |
| | 1 | $BSAGE_{nc}$ | 75.8 | 76.4 | 70.9 | 71.3 | 68.9 |
| | 2 | $BSAGE$ | 77.1 | 89.8 | 83.5 | 73.8 | 81.3 |
| | 3 | V | 89.1 | 93.1 | 79.8 | 65.0 | 81.8 |
| | 4 | $BSAGE + V$ | 91.8 | 93.8 | 84.6 | 66.1 | 83.9 |
| Out-of-domain independent testset | | | $N = 2103$ | $N = 1273$ | $N = 3411$ | $N = 1360$ | $N = 1310$ |
| | 5 | $BSAGE_{nc}$ | 59.4 | 69.0 | 78.3 | 42.9 | 90.1 |
| | 6 | $BSAGE$ | 57.6 | 94.3 | 83.1 | 58.2 | 93.1 |
| | 7 | V | 86.2 | 95.4 | 73.4 | 51.6 | 91.3 |
| | 8 | $BSAGE + V$ | 86.3 | 95.0 | 83.5 | 54.9 | 94.0 |

TABLE A2: Ablation study for binary classification tasks. **Red**: best result, **Blue**: second best result. The area under curve (AUC) is used to assess the model performance (presented in %). We denote $BSAGE_{nc}$, $BSAGE$ and V for respectively $BSAGE$ with no age correction, $BSAGE$ with age correction and structure volume. The validation procedure is presented in Section 3.3.

| | No. | Features | AD vs. CN | FTD vs. CN | MS vs. CN | PD vs. CN | SZ vs. CN |
|--------------------------------------|-----|---------------------|------------|------------|------------|------------|------------|
| In-domain cross-validation | | | $N = 781$ | $N = 547$ | $N = 903$ | $N = 763$ | $N = 614$ |
| | 1 | BSAGE _{nc} | 80.8 | 82.3 | 78.0 | 75.7 | 78.8 |
| | 2 | BSAGE | 94.8 | 94.6 | 91.5 | 79.0 | 88.0 |
| | 3 | V | 95.6 | 95.2 | 87.1 | 71.6 | 88.3 |
| | 4 | BSAGE + V | 96.6 | 97.2 | 93.0 | 72.2 | 91.4 |
| Out-of-domain independent testset | | | $N = 2103$ | $N = 1273$ | $N = 3411$ | $N = 1360$ | $N = 1310$ |
| | 5 | BSAGE _{nc} | 70.1 | 69.5 | 87.3 | 64.9 | 89.8 |
| | 6 | BSAGE | 85.2 | 94.0 | 91.0 | 53.2 | 84.7 |
| | 7 | V | 94.0 | 93.9 | 78.9 | 61.8 | 88.9 |
| | 8 | BSAGE + V | 93.5 | 94.6 | 91.2 | 63.3 | 94.2 |

TABLE A3: Comparison of our model performance with the state-of-the-art methods for the classification CN vs. AD vs. FTD. **Red:** best result, **Blue:** second best result. The results are presented in %. The performance of the state-of-the-art methods is sourced from⁷⁵. It is important to note that the in-domain data used by these methods differs from ours. Specifically, they employed the ADNI2 and NIFD datasets for training their classifiers, whereas we used CN subjects from ADNI2 for training our age prediction models. For training our classifiers, we used all available CN, AD, and FTD samples from our in-domain data. For out-of-domain data, the same dataset (*i.e.*, NACC) with the same subjects as⁷⁵ is employed to ensure a more equitable comparison. It is also worth noting that the table that follows is only presented to offer an overview of the classification efficacy of our framework for CN vs. AD vs. FTD.

| | No. | Methods | BACC | ACC | AUC |
|--------------------------------------|-----|---------------------------|------|------|------|
| In-domain cross-validation | 1 | Hu <i>et al.</i> 2021 | 72.5 | 76.3 | 90.0 |
| | 2 | Ma <i>et al.</i> 2020 | 75.9 | 77.1 | 86.4 |
| | 3 | Nguyen <i>et al.</i> 2023 | 84.4 | 86.0 | 93.8 |
| | 4 | Our method | 85.3 | 88.0 | 95.6 |
| Out-of-domain independent testset | 5 | Hu <i>et al.</i> 2021 | 68.8 | 85.2 | 86.5 |
| | 6 | Ma <i>et al.</i> 2020 | 74.6 | 69.1 | 87.5 |
| | 7 | Nguyen <i>et al.</i> 2023 | 81.6 | 87.1 | 91.6 |
| | 8 | Our method | 82.3 | 84.0 | 91.8 |

TABLE A4: All brain structures with decreasing age gap for each disease. We denote L. for Left, R. for Right.

| AD | | FTD | | MS | |
|----------------------------|--------------|---|--------------|-------------------------------------|--------------|
| Structure | Mean age gap | Structure | Mean age gap | Structure | Mean age gap |
| L. Temporal Pole | 5.23 | L. Temporal Pole | 16.11 | L. Superior Occipital Gyrus | 16.59 |
| L. Amygdala | 5.20 | L. Medial Orbital Gyrus | 15.62 | L. Cun Cuneus | 16.55 |
| L. Posterior Orbital Gyrus | 5.13 | L. Gyrus Rectus | 15.49 | L. Precuneus | 16.42 |
| L. Ent Entorhinal Area | 5.05 | L. Posterior Orbital Gyrus | 15.42 | R. Superior Occipital Gyrus | 16.37 |
| L. Parahippocampal Gyrus | 4.98 | R. Gyrus Rectus | 15.21 | R. Postcentral Gyrus Medial Segment | 16.33 |
| L. Planum Polare | 4.97 | L. Ent Entorhinal Area | 15.03 | R. Superior Frontal Gyrus | 16.23 |
| L. Inferior Temporal Gyrus | 4.96 | L. Anterior Orbital Gyrus | 14.94 | R. Supplementary Motor Cortex | 16.23 |
| L. Hippocampus | 4.90 | R. Anterior Orbital Gyrus | 14.76 | L. Supplementary Motor Cortex | 16.22 |
| L. Anterior Insula | 4.89 | R. Medial Orbital Gyrus | 14.71 | R. Supramarginal Gyrus | 16.19 |
| L. Basal Forebrain | 4.88 | L. Medial Frontal Cortex | 14.68 | R. Cun Cuneus | 16.18 |
| L. Middle Temporal Gyrus | 4.84 | L. Lateral Orbital Gyrus | 14.65 | L. Precentral Gyrus Medial Segment | 16.15 |
| L. Medial Orbital Gyrus | 4.81 | L. Amygdala | 14.63 | R. Planum Temporale | 16.14 |
| L. Fusiform Gyrus | 4.68 | R. Frontal Pole | 14.62 | R. Precentral Gyrus | 16.14 |
| R. Fusiform Gyrus | 4.68 | R. Medial Frontal Cortex | 14.62 | R. Postcentral Gyrus | 16.13 |
| R. Parahippocampal Gyrus | 4.66 | L. Subcallosal Area | 14.41 | R. Precuneus | 16.13 |
| L. Putamen | 4.65 | L. Basal Forebrain | 14.39 | L. Postcentral Gyrus Medial Segment | 16.12 |
| R. Temporal Pole | 4.62 | L. Orbital Part Of The Inferior Frontal Gyrus | 14.36 | L. Posterior Cingulate Gyrus | 16.12 |
| L. Ventral Dc | 4.59 | L. Planum Polare | 14.21 | R. Middle Occipital Gyrus | 16.11 |
| R. Inferior Temporal Gyrus | 4.59 | L. Accumbens Area | 14.19 | R. Superior Parietal Lobule | 16.09 |
| R. Amygdala | 4.57 | R. Temporal Pole | 14.19 | R. Precentral Gyrus Medial Segment | 16.09 |
| L. Posterior Insula | 4.52 | R. Subcallosal Area | 14.12 | R. Angular Gyrus | 16.07 |
| L. Superior Temporal Gyrus | 4.52 | L. Anterior Insula | 13.96 | L. Superior Frontal Gyrus | 16.07 |
| L. Frontal Operculum | 4.52 | R. Basal Forebrain | 13.88 | L. Superior Parietal Lobule | 16.02 |
| R. Middle Temporal Gyrus | 4.50 | R. Ent Entorhinal Area | 13.85 | L. Angular Gyrus | 16.00 |
| R. Planum Polare | 4.46 | R. Lateral Orbital Gyrus | 13.76 | L. Precentral Gyrus | 16.00 |
| External | 4.46 | R. Posterior Orbital Gyrus | 13.69 | L. Middle Cingulate Gyrus | 15.99 |
| R. Hippocampus | 4.45 | L. Inferior Temporal Gyrus | 13.63 | R. Parietal Operculum | 15.94 |
| L. Accumbens Area | 4.44 | L. Frontal Pole | 13.63 | L. Postcentral Gyrus | 15.92 |
| R. Basal Forebrain | 4.42 | L. Frontal Operculum | 13.59 | L. Supramarginal Gyrus | 15.87 |
| L. Inf Lat Vent | 4.39 | L. Putamen | 13.54 | L. Parietal Operculum | 15.86 |
| L. Pallidum | 4.36 | R. Anterior Cingulate Gyrus | 13.51 | L. Middle Occipital Gyrus | 15.80 |
| 4th Ventricle | 4.35 | R. Amygdala | 13.49 | R. Posterior Cingulate Gyrus | 15.80 |
| R. Ent Entorhinal Area | 4.34 | L. Middle Temporal Gyrus | 13.44 | R. Middle Frontal Gyrus | 15.75 |

| | | | | | |
|--|------|--|-------|--|-------|
| R. Posterior Insula | 4.33 | L. Anterior Cingulate Gyrus | 13.39 | L. Middle Frontal Gyrus | 15.73 |
| L. Orbital Part Of The Inferior Frontal Gyrus | 4.33 | L. Superior Temporal Gyrus | 13.25 | R. Middle Cingulate Gyrus | 15.73 |
| R. Superior Temporal Gyrus | 4.33 | R. Superior Frontal Gyrus Medial Segment | 13.18 | L. Superior Frontal Gyrus Medial Segment | 15.71 |
| R. Anterior Insula | 4.32 | L. Parahippocampal Gyrus | 13.18 | L. Lateral Ventricle | 15.61 |
| Brainstem | 4.31 | L. Pallidum | 13.11 | R. Superior Temporal Gyrus | 15.60 |
| L. Transverse Temporal Gyrus | 4.30 | L. Hippocampus | 13.11 | R. Occipital Pole | 15.59 |
| R. Posterior Orbital Gyrus | 4.27 | L. Triangular Part Of The Inferior Frontal Gyrus | 13.10 | L. Opercular Part Of The Inferior Frontal Gyrus | 15.51 |
| R. Ventral De | 4.27 | L. Inf Lat Vent | 13.04 | R. Opercular Part Of The Inferior Frontal Gyrus | 15.48 |
| L. Inferior Occipital Gyrus | 4.26 | L. Posterior Insula | 12.99 | R. Superior Frontal Gyrus Medial Segment | 15.41 |
| R. Transverse Temporal Gyrus | 4.26 | L. Ventral De | 12.92 | L. Central Operculum | 15.41 |
| R. Inf Lat Vent | 4.23 | L. Superior Frontal Gyrus Medial Segment | 12.91 | L. Calc Calcarine Cortex | 15.39 |
| R. Central Operculum | 4.20 | R. Orbital Part Of The Inferior Frontal Gyrus | 12.85 | L. Cerebral White Matter | 15.39 |
| L. Subcallosal Area | 4.20 | L. Opercular Part Of The Inferior Frontal Gyrus | 12.81 | L. Transverse Temporal Gyrus | 15.37 |
| 3rd Ventricle | 4.19 | L. Central Operculum | 12.64 | R. Calc Calcarine Cortex | 15.35 |
| R. Planum Temporale | 4.19 | L. Caudate | 12.62 | L. Planum Temporale | 15.34 |
| R. Anterior Cingulate Gyrus | 4.17 | 3rd Ventricle | 12.60 | R. Central Operculum | 15.29 |
| L. Central Operculum | 4.16 | R. Pallidum | 12.58 | R. Cerebral White Matter | 15.27 |
| R. Anterior Orbital Gyrus | 4.16 | L. Fusiform Gyrus | 12.47 | R. Transverse Temporal Gyrus | 15.27 |
| R. Putamen | 4.11 | L. Transverse Temporal Gyrus | 12.44 | R. Inferior Occipital Gyrus | 15.25 |
| L. Thalamus Proper | 4.10 | R. Anterior Insula | 12.41 | R. Middle Temporal Gyrus | 15.24 |
| R. Pallidum | 4.09 | R. Putamen | 12.41 | R. Lateral Ventricle | 15.14 |
| R. Frontal Operculum | 4.07 | R. Ventral De | 12.40 | L. Triangular Part Of The Inferior Frontal Gyrus | 15.08 |
| R. Opercular Part Of The Inferior Frontal Gyrus | 4.07 | External | 12.38 | L. Thalamus Proper | 15.03 |
| L. Gyrus Rectus | 4.06 | R. Planum Polare | 12.15 | L. Posterior Insula | 15.00 |
| R. Subcallosal Area | 4.06 | R. Superior Frontal Gyrus | 12.14 | L. Caudate | 15.00 |
| L. Opercular Part Of The Inferior Frontal Gyrus | 4.05 | R. Parahippocampal Gyrus | 12.09 | L. Frontal Operculum | 14.91 |
| L. Anterior Orbital Gyrus | 4.05 | L. Lateral Ventricle | 12.09 | L. Anterior Cingulate Gyrus | 14.90 |
| L. Anterior Cingulate Gyrus | 4.04 | L. Middle Frontal Gyrus | 12.08 | L. Occipital Pole | 14.85 |
| R. Cerebellum White Matter | 4.03 | L. Planum Temporale | 12.07 | L. Frontal Pole | 14.79 |
| L. Planum Temporale | 4.02 | L. Superior Frontal Gyrus | 12.04 | R. Posterior Insula | 14.79 |
| R. Lateral Ventricle | 4.01 | R. Triangular Part Of The Inferior Frontal Gyrus | 12.02 | L. Putamen | 14.74 |
| R. Parietal Operculum | 4.01 | R. Middle Frontal Gyrus | 12.00 | External | 14.72 |
| R. Thalamus Proper | 4.00 | R. Middle Cingulate Gyrus | 11.96 | L. Pallidum | 14.63 |
| R. Superior Frontal Gyrus Medial Segment | 3.99 | Brainstem | 11.89 | R. Triangular Part Of The Inferior Frontal Gyrus | 14.61 |
| R. Cerebral White Matter | 3.98 | R. Frontal Operculum | 11.86 | L. Anterior Insula | 14.58 |
| L. Cerebellum White Matter | 3.97 | L. Thalamus Proper | 11.81 | L. Orbital Part Of The Inferior Frontal Gyrus | 14.57 |
| R. Cerebellum Exterior | 3.95 | L. Middle Cingulate Gyrus | 11.80 | L. Superior Temporal Gyrus | 14.56 |
| L. Lateral Ventricle | 3.95 | R. Supplementary Motor Cortex | 11.77 | R. Frontal Operculum | 14.54 |
| R. Inferior Occipital Gyrus | 3.95 | L. Cerebral White Matter | 11.76 | L. Lateral Orbital Gyrus | 14.52 |
| R. Medial Orbital Gyrus | 3.94 | R. Lateral Ventricle | 11.76 | R. Anterior Cingulate Gyrus | 14.48 |
| L. Medial Frontal Cortex | 3.94 | R. Hippocampus | 11.73 | R. Anterior Insula | 14.40 |
| R. Occipital Fusiform Gyrus | 3.92 | R. Accumbens Area | 11.70 | R. Frontal Pole | 14.38 |
| R. Medial Frontal Cortex | 3.92 | R. Opercular Part Of The Inferior Frontal Gyrus | 11.67 | L. Anterior Orbital Gyrus | 14.36 |
| R. Orbital Part Of The Inferior Frontal Gyrus | 3.92 | R. Inferior Temporal Gyrus | 11.60 | L. Planum Polare | 14.35 |
| Cerebellar Vermal Lobules I-v | 3.91 | L. Supplementary Motor Cortex | 11.53 | R. Planum Polare | 14.35 |
| L. Triangular Part Of The Inferior Frontal Gyrus | 3.90 | R. Thalamus Proper | 11.53 | R. Putamen | 14.28 |
| L. Caudate | 3.89 | L. Parietal Operculum | 11.46 | R. Caudate | 14.24 |
| R. Gyrus Rectus | 3.89 | R. Posterior Insula | 11.37 | R. Lingual Gyrus | 14.18 |
| R. Accumbens Area | 3.86 | R. Fusiform Gyrus | 11.37 | R. Thalamus Proper | 14.18 |
| R. Caudate | 3.86 | L. Precentral Gyrus | 11.36 | R. Pallidum | 14.05 |
| R. Middle Cingulate Gyrus | 3.86 | R. Inf Lat Vent | 11.29 | R. Orbital Part Of The Inferior Frontal Gyrus | 14.02 |
| L. Lateral Orbital Gyrus | 3.85 | R. Cerebral White Matter | 11.24 | L. Lingual Gyrus | 13.96 |
| R. Lateral Orbital Gyrus | 3.84 | R. Central Operculum | 11.18 | L. Medial Orbital Gyrus | 13.94 |
| L. Cerebral White Matter | 3.83 | R. Middle Temporal Gyrus | 11.05 | L. Medial Frontal Cortex | 13.92 |
| Cerebellar Vermal Lobules Viii-x | 3.80 | L. Cerebellum White Matter | 11.05 | L. Gyrus Rectus | 13.91 |
| R. Middle Frontal Gyrus | 3.79 | R. Precentral Gyrus | 10.93 | L. Accumbens Area | 13.87 |
| R. Lingual Gyrus | 3.77 | 4th Ventricle | 10.86 | R. Inferior Temporal Gyrus | 13.83 |
| Cerebellar Vermal Lobules Vi-vii | 3.76 | L. Inferior Occipital Gyrus | 10.84 | L. Middle Temporal Gyrus | 13.82 |
| L. Parietal Operculum | 3.75 | R. Precentral Gyrus Medial Segment | 10.82 | R. Temporal Pole | 13.81 |
| R. Triangular Part Of The Inferior Frontal Gyrus | 3.74 | L. Supramarginal Gyrus | 10.80 | R. Lateral Orbital Gyrus | 13.79 |
| L. Superior Frontal Gyrus Medial Segment | 3.72 | R. Superior Temporal Gyrus | 10.79 | 3rd Ventricle | 13.74 |
| L. Middle Cingulate Gyrus | 3.71 | L. Postcentral Gyrus | 10.74 | R. Posterior Orbital Gyrus | 13.70 |
| R. Middle Occipital Gyrus | 3.69 | R. Transverse Temporal Gyrus | 10.69 | R. Occipital Fusiform Gyrus | 13.67 |
| L. Middle Occipital Gyrus | 3.68 | L. Precentral Gyrus Medial Segment | 10.64 | L. Posterior Orbital Gyrus | 13.64 |
| R. Calc Calcarine Cortex | 3.65 | L. Cerebellum Exterior | 10.49 | L. Temporal Pole | 13.62 |
| L. Occipital Fusiform Gyrus | 3.63 | L. Posterior Cingulate Gyrus | 10.47 | R. Anterior Orbital Gyrus | 13.61 |
| R. Frontal Pole | 3.61 | R. Posterior Cingulate Gyrus | 10.43 | R. Medial Frontal Cortex | 13.58 |
| L. Cerebellum Exterior | 3.60 | L. Middle Occipital Gyrus | 10.35 | L. Inferior Occipital Gyrus | 13.53 |
| R. Precentral Gyrus | 3.60 | L. Angular Gyrus | 10.34 | R. Gyrus Rectus | 13.53 |
| L. Lingual Gyrus | 3.57 | R. Caudate | 10.32 | R. Inf Lat Vent | 13.44 |
| R. Supramarginal Gyrus | 3.56 | L. Occipital Fusiform Gyrus | 10.30 | L. Hippocampus | 13.40 |
| R. Posterior Cingulate Gyrus | 3.53 | R. Parietal Operculum | 10.28 | R. Hippocampus | 13.40 |
| R. Angular Gyrus | 3.49 | R. Cerebellum White Matter | 10.27 | L. Ventral De | 13.37 |
| R. Supplementary Motor Cortex | 3.47 | Cerebellar Vermal Lobules I-v | 10.23 | R. Medial Orbital Gyrus | 13.33 |
| R. Superior Frontal Gyrus | 3.46 | R. Planum Temporale | 10.17 | L. Inf Lat Vent | 13.33 |
| R. Precentral Gyrus Medial Segment | 3.38 | R. Postcentral Gyrus | 10.11 | L. Subcallosal Area | 13.32 |
| L. Posterior Cingulate Gyrus | 3.31 | Cerebellar Vermal Lobules Viii-x | 10.08 | L. Basal Forebrain | 13.29 |
| R. Cun Cuneus | 3.29 | R. Postcentral Gyrus Medial Segment | 10.07 | R. Fusiform Gyrus | 13.29 |
| L. Calc Calcarine Cortex | 3.26 | L. Postcentral Gyrus Medial Segment | 10.04 | R. Ent Entorhinal Area | 13.20 |
| R. Postcentral Gyrus | 3.25 | L. Superior Parietal Lobule | 10.03 | R. Accumbens Area | 13.16 |
| L. Middle Frontal Gyrus | 3.18 | R. Cerebellum Exterior | 9.93 | R. Subcallosal Area | 13.06 |
| L. Supplementary Motor Cortex | 3.17 | L. Precuneus | 9.91 | L. Amygdala | 13.01 |
| R. Precuneus | 3.16 | L. Lingual Gyrus | 9.89 | L. Ent Entorhinal Area | 12.99 |
| R. Superior Occipital Gyrus | 3.14 | R. Precuneus | 9.85 | R. Parahippocampal Gyrus | 12.98 |
| L. Superior Frontal Gyrus | 3.11 | R. Supramarginal Gyrus | 9.82 | R. Basal Forebrain | 12.93 |
| L. Frontal Pole | 3.01 | Cerebellar Vermal Lobules Vi-vii | 9.57 | Cerebellar Vermal Lobules I-v | 12.90 |
| L. Supramarginal Gyrus | 2.94 | R. Angular Gyrus | 9.53 | R. Ventral De | 12.89 |
| L. Precentral Gyrus Medial Segment | 2.94 | R. Inferior Occipital Gyrus | 9.52 | R. Amygdala | 12.82 |
| L. Angular Gyrus | 2.94 | R. Occipital Fusiform Gyrus | 9.46 | L. Parahippocampal Gyrus | 12.72 |
| L. Cun Cuneus | 2.88 | R. Lingual Gyrus | 9.43 | L. Inferior Temporal Gyrus | 12.54 |
| R. Postcentral Gyrus Medial Segment | 2.86 | R. Superior Parietal Lobule | 9.35 | L. Fusiform Gyrus | 12.23 |
| L. Precuneus | 2.86 | L. Calc Calcarine Cortex | 9.34 | R. Cerebellum White Matter | 12.22 |
| L. Superior Occipital Gyrus | 2.85 | R. Calc Calcarine Cortex | 9.16 | R. Cerebellum Exterior | 12.12 |
| L. Precentral Gyrus | 2.83 | R. Middle Occipital Gyrus | 9.16 | L. Occipital Fusiform Gyrus | 12.11 |
| R. Superior Parietal Lobule | 2.60 | L. Superior Occipital Gyrus | 9.14 | Brainstem | 12.08 |

| | | | | | |
|-------------------------------------|------|-----------------------------|------|----------------------------------|-------|
| L. Occipital Pole | 2.59 | R. Cun Cuneus | 9.05 | Cerebellar Vermal Lobules Vi-vii | 11.94 |
| L. Postcentral Gyrus | 2.58 | L. Cun Cuneus | 8.99 | Cerebellar Vermal Lobules Viii-x | 11.56 |
| L. Postcentral Gyrus Medial Segment | 2.51 | R. Superior Occipital Gyrus | 8.53 | L. Cerebellum White Matter | 11.47 |
| L. Superior Parietal Lobule | 2.33 | L. Occipital Pole | 7.78 | 4th Ventricle | 11.37 |
| R. Occipital Pole | 2.21 | R. Occipital Pole | 7.59 | L. Cerebellum Exterior | 10.88 |

| PD | | SZ | |
|--|--------------|--|--------------|
| Structure | Mean age gap | Structure | Mean age gap |
| R. Lateral Orbital Gyrus | 2.58 | L. Lateral Orbital Gyrus | 13.09 |
| R. Frontal Pole | 2.56 | L. Anterior Orbital Gyrus | 12.46 |
| R. Anterior Orbital Gyrus | 2.39 | L. Temporal Pole | 11.97 |
| R. Orbital Part Of The Inferior Frontal Gyrus | 2.25 | L. Frontal Pole | 11.79 |
| R. Medial Orbital Gyrus | 2.24 | L. Orbital Part Of The Inferior Frontal Gyrus | 11.55 |
| R. Middle Frontal Gyrus | 2.17 | L. Gyrus Rectus | 11.40 |
| R. Triangular Part Of The Inferior Frontal Gyrus | 2.15 | L. Posterior Orbital Gyrus | 11.29 |
| R. Superior Frontal Gyrus | 2.15 | R. Frontal Pole | 11.26 |
| R. Medial Frontal Cortex | 2.06 | L. Medial Orbital Gyrus | 11.13 |
| R. Gyrus Rectus | 1.97 | R. Anterior Orbital Gyrus | 11.13 |
| R. Postcentral Gyrus Medial Segment | 1.96 | L. Middle Frontal Gyrus | 11.03 |
| R. Precentral Gyrus Medial Segment | 1.93 | R. Lateral Orbital Gyrus | 10.97 |
| R. Precentral Gyrus | 1.92 | R. Gyrus Rectus | 10.80 |
| L. Gyrus Rectus | 1.91 | R. Temporal Pole | 10.63 |
| R. Posterior Orbital Gyrus | 1.91 | L. Medial Frontal Cortex | 10.59 |
| R. Supplementary Motor Cortex | 1.88 | L. Triangular Part Of The Inferior Frontal Gyrus | 10.54 |
| R. Temporal Pole | 1.86 | L. Ent Entorhinal Area | 10.39 |
| L. Frontal Pole | 1.84 | R. Medial Orbital Gyrus | 10.20 |
| R. Opercular Part Of The Inferior Frontal Gyrus | 1.84 | R. Posterior Orbital Gyrus | 10.17 |
| R. Superior Frontal Gyrus Medial Segment | 1.84 | L. Opercular Part Of The Inferior Frontal Gyrus | 10.11 |
| R. Anterior Cingulate Gyrus | 1.81 | L. Supramarginal Gyrus | 10.05 |
| L. Medial Frontal Cortex | 1.78 | L. Precentral Gyrus | 10.04 |
| L. Superior Frontal Gyrus Medial Segment | 1.77 | L. Superior Frontal Gyrus | 10.00 |
| R. Postcentral Gyrus | 1.77 | R. Medial Frontal Cortex | 9.96 |
| R. Subcallosal Area | 1.77 | L. Planum Polare | 9.94 |
| R. Caudate | 1.70 | L. Anterior Insula | 9.89 |
| R. Frontal Operculum | 1.70 | L. Angular Gyrus | 9.86 |
| R. Accumbens Area | 1.66 | L. Postcentral Gyrus | 9.83 |
| L. Anterior Cingulate Gyrus | 1.64 | R. Orbital Part Of The Inferior Frontal Gyrus | 9.82 |
| R. Anterior Insula | 1.64 | L. Frontal Operculum | 9.76 |
| R. Basal Forebrain | 1.61 | R. Ent Entorhinal Area | 9.69 |
| L. Middle Frontal Gyrus | 1.59 | R. Middle Frontal Gyrus | 9.67 |
| L. Supplementary Motor Cortex | 1.58 | R. Superior Frontal Gyrus | 9.66 |
| R. Superior Parietal Lobule | 1.54 | L. Basal Forebrain | 9.48 |
| L. Superior Frontal Gyrus | 1.53 | L. Parietal Operculum | 9.48 |
| R. Ent Entorhinal Area | 1.52 | L. Amygdala | 9.46 |
| L. Precentral Gyrus Medial Segment | 1.51 | External | 9.45 |
| R. Pallidum | 1.51 | L. Superior Temporal Gyrus | 9.39 |
| R. Putamen | 1.47 | L. Middle Temporal Gyrus | 9.37 |
| R. Middle Cingulate Gyrus | 1.44 | R. Inferior Temporal Gyrus | 9.35 |
| R. Amygdala | 1.43 | L. Central Operculum | 9.32 |
| R. Planum Polare | 1.43 | L. Subcallosal Area | 9.29 |
| L. Medial Orbital Gyrus | 1.38 | L. Inferior Temporal Gyrus | 9.26 |
| External | 1.36 | L. Posterior Insula | 9.24 |
| L. Anterior Orbital Gyrus | 1.36 | L. Superior Frontal Gyrus Medial Segment | 9.20 |
| R. Cerebral White Matter | 1.36 | L. Supplementary Motor Cortex | 9.20 |
| L. Postcentral Gyrus Medial Segment | 1.35 | L. Planum Temporale | 9.20 |
| L. Triangular Part Of The Inferior Frontal Gyrus | 1.33 | L. Middle Occipital Gyrus | 9.07 |
| R. Central Operculum | 1.32 | R. Triangular Part Of The Inferior Frontal Gyrus | 9.07 |
| L. Subcallosal Area | 1.30 | R. Middle Temporal Gyrus | 9.06 |
| L. Middle Cingulate Gyrus | 1.28 | L. Superior Parietal Lobule | 9.05 |
| L. Orbital Part Of The Inferior Frontal Gyrus | 1.27 | L. Transverse Temporal Gyrus | 8.91 |
| L. Lateral Orbital Gyrus | 1.25 | R. Opercular Part Of The Inferior Frontal Gyrus | 8.87 |
| L. Accumbens Area | 1.24 | L. Inf Lat Vent | 8.85 |
| R. Posterior Insula | 1.24 | L. Cerebral White Matter | 8.81 |
| L. Basal Forebrain | 1.24 | R. Subcallosal Area | 8.76 |
| R. Precuneus | 1.23 | R. Superior Temporal Gyrus | 8.75 |
| R. Lateral Ventricle | 1.21 | R. Planum Polare | 8.74 |
| L. Caudate | 1.19 | L. Postcentral Gyrus Medial Segment | 8.74 |
| 3rd Ventricle | 1.19 | R. Supplementary Motor Cortex | 8.70 |
| R. Inf Lat Vent | 1.17 | R. Amygdala | 8.70 |
| L. Frontal Operculum | 1.15 | R. Anterior Insula | 8.66 |
| R. Ventral Dc | 1.11 | R. Precentral Gyrus | 8.65 |
| L. Temporal Pole | 1.08 | L. Precentral Gyrus Medial Segment | 8.65 |
| L. Opercular Part Of The Inferior Frontal Gyrus | 1.08 | L. Superior Occipital Gyrus | 8.64 |
| R. Thalamus Proper | 1.07 | L. Accumbens Area | 8.63 |
| L. Anterior Insula | 1.05 | R. Occipital Pole | 8.49 |
| L. Pallidum | 1.03 | R. Superior Frontal Gyrus Medial Segment | 8.45 |
| L. Posterior Orbital Gyrus | 1.02 | R. Superior Occipital Gyrus | 8.42 |
| R. Posterior Cingulate Gyrus | 1.02 | L. Parahippocampal Gyrus | 8.41 |
| R. Parahippocampal Gyrus | 1.01 | R. Basal Forebrain | 8.38 |
| R. Transverse Temporal Gyrus | 0.97 | R. Fusiform Gyrus | 8.37 |
| L. Amygdala | 0.96 | R. Frontal Operculum | 8.36 |
| L. Putamen | 0.95 | L. Putamen | 8.31 |
| R. Hippocampus | 0.95 | L. Anterior Cingulate Gyrus | 8.31 |
| R. Parietal Operculum | 0.94 | L. Hippocampus | 8.30 |
| L. Precentral Gyrus | 0.94 | R. Inf Lat Vent | 8.26 |
| R. Inferior Temporal Gyrus | 0.92 | L. Cun Cuneus | 8.20 |
| L. Ventral Dc | 0.89 | R. Inferior Occipital Gyrus | 8.17 |
| L. Ent Entorhinal Area | 0.88 | R. Planum Temporale | 8.13 |
| R. Supramarginal Gyrus | 0.86 | R. Postcentral Gyrus | 8.08 |
| R. Superior Temporal Gyrus | 0.83 | L. Fusiform Gyrus | 8.07 |
| L. Lateral Ventricle | 0.83 | R. Central Operculum | 8.05 |

| | | | |
|----------------------------------|-------|-------------------------------------|------|
| L. Precuneus | 0.81 | R. Precentral Gyrus Medial Segment | 8.03 |
| L. Planum Polare | 0.75 | R. Postcentral Gyrus Medial Segment | 7.96 |
| Brainstem | 0.73 | L. Precuneus | 7.95 |
| L. Thalamus Proper | 0.71 | R. Middle Occipital Gyrus | 7.91 |
| R. Middle Temporal Gyrus | 0.71 | R. Posterior Insula | 7.84 |
| R. Planum Temporale | 0.69 | R. Cerebral White Matter | 7.80 |
| L. Superior Parietal Lobule | 0.68 | R. Parietal Operculum | 7.80 |
| L. Posterior Cingulate Gyrus | 0.68 | R. Parahippocampal Gyrus | 7.76 |
| L. Cerebral White Matter | 0.68 | R. Cun Cuneus | 7.68 |
| R. Angular Gyrus | 0.62 | R. Hippocampus | 7.65 |
| L. Parahippocampal Gyrus | 0.61 | R. Occipital Fusiform Gyrus | 7.63 |
| R. Cun Cuneus | 0.59 | R. Anterior Cingulate Gyrus | 7.62 |
| L. Postcentral Gyrus | 0.56 | R. Supramarginal Gyrus | 7.60 |
| L. Central Operculum | 0.54 | R. Superior Parietal Lobule | 7.55 |
| L. Posterior Insula | 0.51 | R. Cerebellum Exterior | 7.55 |
| R. Fusiform Gyrus | 0.50 | L. Occipital Pole | 7.52 |
| L. Inf Lat Vent | 0.50 | R. Accumbens Area | 7.51 |
| L. Hippocampus | 0.50 | R. Putamen | 7.49 |
| R. Calc Calcarine Cortex | 0.37 | L. Pallidum | 7.46 |
| R. Cerebellum White Matter | 0.35 | L. Middle Cingulate Gyrus | 7.42 |
| 4th Ventricle | 0.34 | Brainstem | 7.35 |
| Cerebellar Vermal Lobules I-v | 0.28 | L. Caudate | 7.33 |
| R. Lingual Gyrus | 0.25 | R. Transverse Temporal Gyrus | 7.32 |
| R. Superior Occipital Gyrus | 0.21 | L. Ventral Dc | 7.30 |
| L. Cun Cuneus | 0.20 | L. Inferior Occipital Gyrus | 7.24 |
| L. Transverse Temporal Gyrus | 0.14 | L. Posterior Cingulate Gyrus | 7.20 |
| Cerebellar Vermal Lobules Viii-x | 0.14 | R. Angular Gyrus | 7.19 |
| L. Inferior Temporal Gyrus | 0.13 | R. Precuneus | 7.19 |
| R. Cerebellum Exterior | 0.06 | R. Cerebellum White Matter | 7.17 |
| R. Middle Occipital Gyrus | 0.00 | L. Calc Calcarine Cortex | 7.16 |
| R. Inferior Occipital Gyrus | -0.02 | L. Lateral Ventricle | 7.09 |
| R. Occipital Pole | -0.03 | 4th Ventricle | 7.02 |
| L. Cerebellum White Matter | -0.04 | L. Cerebellum White Matter | 6.99 |
| R. Occipital Fusiform Gyrus | -0.04 | R. Middle Cingulate Gyrus | 6.97 |
| L. Superior Temporal Gyrus | -0.04 | R. Calc Calcarine Cortex | 6.96 |
| L. Fusiform Gyrus | -0.08 | R. Pallidum | 6.75 |
| Cerebellar Vermal Lobules Vi-vii | -0.12 | 3rd Ventricle | 6.72 |
| L. Middle Temporal Gyrus | -0.14 | L. Lingual Gyrus | 6.71 |
| L. Calc Calcarine Cortex | -0.18 | R. Posterior Cingulate Gyrus | 6.67 |
| L. Lingual Gyrus | -0.19 | Cerebellar Vermal Lobules Viii-x | 6.65 |
| L. Parietal Operculum | -0.22 | R. Ventral Dc | 6.64 |
| L. Planum Temporale | -0.24 | L. Cerebellum Exterior | 6.63 |
| L. Supramarginal Gyrus | -0.35 | R. Lingual Gyrus | 6.59 |
| L. Superior Occipital Gyrus | -0.38 | Cerebellar Vermal Lobules I-v | 6.54 |
| L. Angular Gyrus | -0.42 | R. Lateral Ventricle | 6.41 |
| L. Cerebellum Exterior | -0.48 | R. Caudate | 6.34 |
| L. Occipital Pole | -0.78 | L. Thalamus Proper | 6.26 |
| L. Middle Occipital Gyrus | -0.92 | Cerebellar Vermal Lobules Vi-vii | 6.20 |
| L. Occipital Fusiform Gyrus | -1.01 | L. Occipital Fusiform Gyrus | 5.88 |
| L. Inferior Occipital Gyrus | -1.30 | R. Thalamus Proper | 5.51 |